A New Empirical Potential Energy Function for Ar_2

Philip T. Myatt,[1] Ashok K. Dham,[2,1] Pragna Chandrasekhar,[1]
Frederick R. W. McCourt,[1] and Robert J. Le Roy[1]*

[1] *Department of Chemistry,*
University of Waterloo, Waterloo,
Ontario N2L 3G1, Canada

[2] *Department of Physics,*
Punjabi University, Patiala 147002, India

* *leroy@uwaterloo.ca*

A critical re-analysis of all available spectroscopic and virial coefficient data for Ar_2 has been used to determine an improved empirical analytic potential energy function that has been 'tuned' to optimize its agreement with viscosity, diffusion, and thermal diffusion data, and whose short-range behaviour is in reasonably good agreement with the most recent *ab initio* calculations for this system. The recommended Morse/long-Range (MLR) potential function is smooth and differentiable at all distances, and incorporates both the correct theoretically predicted long-range behaviour and the correct limiting short-range functional behaviour. The resulting value of the well depth is $\mathfrak{D}_e = 99.49\,(\pm 0.04)$ cm^{-1} and the associated equilibrium distance is $r_e = 3.766\,(\pm 0.002)$ Å, while the ^{40}Ar s-wave scattering length is -714 Å.

Keywords

Ar_2 potential curve, Ar_2 virial coefficients, Ar_2 transport coefficients, empirical analysis

1. Introduction

Diatomic molecules in their ground electronic states may be assigned fairly readily to one of two distinct classes, one being chemically bound species with deep potential energy wells that support numerous excited vibrational and rotational energy levels, the other being physically bound (Van der Waals) species which generally have quite shallow potential energy wells that support relatively few vibrational and rotational levels. The former class is typified by diatomic molecules formed by pairs of open-shell atoms, while the latter is typified by diatomic molecules formed by pairs of closed-shell atoms, in particular, noble gas and alkaline earth atoms. Diatomic molecules formed from pairs of open s-shell atoms, such as hydrogen or alkali atoms, have both chemically-bound ground singlet electronic states and weakly-bound excited triplet 'Van der Waals' electronic states sharing the same dissociation asymptote. By and large, the development of characteristic functional forms to represent interaction energies between atom pairs of these two classes of species followed separate paths. This ultimately unnecessary distinction between intramolecular and intermolecular interactions for (diatomic) molecules was reinforced by the fact that copious amounts of vibration-rotation spectroscopic data tended to be available for 'chemically bound' species, while relatively fewer data were available for 'physically bound' species.

Representation of the interaction energy between a pair of closed-shell atoms has a long history, beginning with the rather simplistic (and unrealistic) fifth-power repulsive force law introduced by Maxwell [1] in the 19^{th} century, followed by introduction of simple two-term repulsive-attractive representations of the interaction energy introduced during the first half of the 20^{th} century, as exemplified by the two-parameter (Lennard-)Jones (LJ) [2, 3] and exponential-six (exp-6) [4, 5] models, both of which incorporated the form of the leading inverse-power dispersion energy term associated with pairs of closed-shell atoms. The most common LJ potential energy function, characterized by a minimum at energy $-\mathfrak{D}_{\text{e}}$ and radial position r_{e}, is the sum of a repulsive term that varies with atomic separation r as r^{-12} and an attractive term that varies as r^{-6}. However, it was realized soon after the introduction of the LJ model in 1924 that, while such a simple two-term inverse-power form was adequate for describing the relatively imprecise experimental virial and transport coefficients available at the time, it was wholly inadequate for describing the much more precise measurements of spectroscopic transition frequencies of chemically-bound diatomic molecules. This led to people thinking of intramolecular and intermolecular interaction energies in qualitatively, rather than only quantitatively, different manners. Indeed, in 1929, Morse [6] proposed the two-term three-parameter functional form now known as the Morse potential, in which exponential functions were employed to represent both repulsive and attractive branches of the interaction energy between pairs of (open-shell) atoms, and showed that it provided an adequate description of most of the then-available diatomic molecular vibrational spectroscopic data.

Although early second virial and viscosity coefficients were available over reasonably extensive temperature ranges, they could still adequately be described in terms of simple two-parameter models of the LJ form because their values could only be determined within experimental uncertainties of the order of a few percent. Once experimental uncertainties were reduced to fractions of one

percent, such overly simple forms were no longer adequate, and more sophisticated functional forms were required. For example, the two-parameter LJ model was modified to give a three-parameter extended LJ model [7] in which the inverse power of the long-range attractive term was fixed at six while the inverse power of the repulsive term was replaced by a constrained linear function of the interatomic separation, and this model sufficed to provide a consistent rendering of the temperature dependences of the available second (pressure) virial coefficient and transport coefficients. More realistic representations of both the repulsive and attractive components of the interaction energy based upon theoretical constraints were also introduced around the same time. Of particular note were the multiparameter Hartree-Fock plus damped dispersion (HFD) [8, 9] and exchange-Coulomb (XC) [10, 11] models. Although the most recent multiparameter versions of these functional forms for the potential energy may readily be tuned to give good representations of the temperature dependences of both second virial and bulk transport properties, it proved to be considerably more challenging to obtain unique accurate functional representation of *all* properties.

It should also be pointed out that even though quantum chemical computational methods have recently become able to provide rather accurate *ab initio* pair interaction energies, for all but the smallest chemically-bound species (e.g., H_2 and H_2^+) they are still not sufficiently accurate to be able to predict spectroscopic transitions with a precision that matches experiment. Consequently, empirical potential energy functional forms remain the mainstay for the determination of highly accurate interaction energies for chemically-bound diatomic species. The most accurate available *ab initio* interaction energies for the ground electronic states of noble gas pairs, specifically He_2 [12, 13], Ne_2 [14], and Ar_2 [15, 16], give excellent agreement with experimental values of the virial and transport coefficients of these bulk gases, and give good agreement with vibrational level spacings deduced from spectroscopic data. However, it has not yet been demonstrated clearly that the best published *ab initio* $Ar_2(X\,^1\Sigma_g^+)$ potential energy functions [15, 16] are sufficiently accurate to give directly computed spectroscopic transition energies that lie within the reported experimental uncertainties (see, however, § 5.1).

It has been well established that the shapes and radial positions of potential energy functions for chemically-bound diatomic molecules in their ground electronic states are most accurately determined from analyses of the transition energies associated with their allowed spectroscopic transitions amongst the plethora of molecular states possessed by stable molecules. A number of different representations of the potential energy function (PEF) for a diatomic molecule have been proposed over the years, arguably beginning with the Morse PEF [6] in 1929. The Morse PEF was followed in 1932 by Dunham's introduction of a PEF written as a polynomial in powers of a dimensionless radial variable [17], together with analytic expressions relating the lower-order coefficients of the polynomial PEF to the coefficients of empirically-determined polynomial expressions representing the molecular energy levels as double power series in the vibrational and rotational quantum numbers. For much of the next half century, spectroscopic data analyses focussed upon performing empirical fits to the Dunham double-power-series expansion and, from the mid 1960s onward, generating sets of turning points from the resulting functions using the semiclassical Rydberg-Klein-Rees [18] (RKR) procedure. However, relatively little attention was paid to finding more appropriate analytic

forms for the underlying PEFs.

A key subsequent development in analytic functional forms for chemically bound molecules was due to Coxon and Hajigeorgiou [19], who showed that a Morse-type PEF with an exponent coefficient that varied with distance was an extremely flexible form that required substantially fewer parameters to represent a given spectroscopic data set accurately than did an equivalent Dunham expansion. Replacing its radial distance variable by a dimensionless radial variable [20, 21] that maps the semi-infinite domain $[0, \infty)$ onto the finite domain [-1,+1], and introduction of a dimensionless prefactor to the exponential term [22] that enables the PEF to have any specified long-range tail behaviour [23–25] then yielded the 'Morse/Long-Range' (MLR) PEF form [25, 26].

MLR PEFs have been employed successfully to obtain excellent representations of large, and often diverse spectroscopic data sets for a variety of ground and excited state species, such as N_2 [27], MgH(D) [23, 28], Li_2 [24], hydrogen halides [29], and CH^+ [30]. Moreover, such studies have also provided excellent representations of both 'conventionally shallow' Van der Waals potentials such as the $a\,^3\Sigma_u^+$ state of Li_2 [31], and the ground states of the semi-chemically bound Van der Waals species Be_2 [32] and Mg_2 [33]. This functional form has been selected for the present redetermination of the potential energy function for the $X\,^1\Sigma_g^+$ state of Ar_2.

It wasn't until 1970, when Tanaka and Yoshino [34] reported their first measurements of electronic transitions in argon, that discrete vibrational spectroscopic data became available for a noble gas diatomic species. However, their vibrational band-head measurements sufficed only to determine the energies of six of the nine [35] vibrational levels of ground-state Ar_2. A few years later, a similar study employing a higher-resolution spectrograph that delineated the rotational structure of those same six vibrational levels of Ar_2 allowed Colbourn and Douglas [36] to obtain a RKR potential for ground-state Ar_2, to which they attached an analytic long-range tail consisting of a sum of inverse-power terms. A decade later, Herman *et. al.* [37] utilized high-resolution VUV emission from three excited electronic (excimer) states of Ar_2 to obtain improved values of the band constants and relative ro-vibrational level energies for $v = 0, \cdots, 5$ of the electronic ground state plus a number of vibrational levels for three excited electronic states.

Gaseous argon has played an important role as one of the key substances utilized for establishing benchmark standards for equation-of-state and transport property measurements. For this reason, there has been a strong interest in obtaining a highly accurate pair interaction potential energy function for its ground electronic ($X\,^1\Sigma_g^+$) state. The first serious attempt to attain this goal was carried out by Barker and coworkers [38–40], having shown conclusively [41, 42] that both the popular LJ and exp-6 model functional forms were inadequate. As new microscopic [34, 36, 43, 44] and bulk [45–47] experimental data, plus more extensive and/or accurate [48–54] experimental transport data became available for argon, more sophisticated functional forms, especially of the HFD-type [8, 9], began to be employed rather successfully [55–57] to represent the dependence of the potential energy, $V(r)$, on the separation, r, between a pair of ground-electronic-state Ar atoms. However, much of that work consisted of manual (trial-and-error) fits, and none of it combined fully quantum simulations of the actual spectroscopic data together with high-level simulations of the bulk property measurements in a unified non-linear least-squares fit analysis. The present work

describes such an analysis and determines an improved empirical analytic potential energy function for ground-state Ar_2.

Over the past decade or so, significant improvements in both computer hardware and quantum chemical methodology (reviewed extensively in Refs. [15] and [16]) have enabled increasingly accurate *ab initio* computations of $V(r)$ for the Ar_2 dimer [58–65], culminating in the essentially converged results reported in Refs. [15] and [16], both of which were fitted to (different) multi-parameter modifications of the TT version [9] of the HFD functional form. In contrast, the present work will provide what will hopefully be the final and "best" *empirical* potential, against which such calculations may be tested.

2. Empirical Determination of Diatomic Potential Energy Functions

Chemically-bound diatomic molecules typically support large numbers of vibrational and rotational levels in their electronic ground states, which in principle allows a wealth of pure rotational and ro-vibration data, as well as electronic ro-vibrational data, to be obtained and utilized for the determination of accurate potential energy functions. Since the turn of the present century this process has increasingly involved the application of robust numerical Schrödinger-solver computer programs to preliminary, but realistic, parameterized analytic model functions $V(r;\{p_j\})$ to generate estimates of the energies $\overline{E}(v'J')$ and $\overline{E}(v'',J'')$, of the upper, respectively, lower energy levels (expressed in cm^{-1} units) associated with each experimentally-reported spectroscopic transition. This process yields a set of simulated transition energies

$$\overline{\nu}_{\rm calc}(v',J';v'',J'') \;=\; \overline{E}(v',J') - \overline{E}(v'',J'') \quad , \tag{1}$$

for comparison with the corresponding experimental data (traditionally given as a set of wave-number values). An optimized analytic PEF may then be obtained by carrying out a sequential fitting routine that involves a systematic variation of the set of potential parameters $\{p_j\}$ in order to minimize the root-mean-square deviation (RMSD) between simulated and experimental results. This procedure is facilitated by the fact that the Schrödinger solver that yields an eigenvalue $E(v,J)$ normally also yields the associated eigenfunction $\psi_{v,J}(r)$, which in turn allows the Hellmann-Feynman theorem expression

$$\frac{\partial E(v,J)}{\partial p_j} \;=\; \left\langle \psi_{v,J} \left| \frac{\partial V(r;\{p_j\})}{\partial p_j} \right| \psi_{v,J} \right\rangle$$

to be used for efficient calculation of the partial derivatives with respect to the potential function parameters $\{p_j\}$ required for the least-squares parameter-optimization procedure.

Because it remains a well-entrenched tradition in both the spectroscopic and potential energy function/surface research communities to report spectroscopic transitions and potential energies in terms of wave-numbers and cm^{-1} units and to report wavelengths and separations in Ångstrom (Å) units, we have chosen to conform with this tradition.

Physically-bound diatomic molecules support many fewer bound vibrational and rotational levels than do chemically-bound diatomic molecules, with a consequent reduction in the number of spectroscopic transitions available for observation and analysis. As dipole moments and dipole-moment-derivatives for such molecules tend to be small, pure rotational and rovibrational transitions are relatively weak. Moreover, their typically rather small binding energies results in their thermal populations being quite low in most environments. Hence, the amount of highly accurate spectroscopic data available is often insufficient to enable a fully reliable empirical PEF for the atom-atom potential energy well to be obtained by fitting to them alone. In any case, such eigenvalue differences would only be directly sensitive to the PEF at energies below the dissociation asymptote, so that interaction energies for separations smaller than the location, σ, of the (finite-separation) zero of $V(r)$ cannot be determined directly from discrete spectroscopic data.

As short-range interaction energies between pairs of rare gas atoms play significant roles in determining bulk properties of these species, it is important to incorporate experimental data that are influenced by the nature of the repulsive wall of the PEF into the fitting procedure. Fortunately, bulk-gas phenomena, such as equation-of-state and acoustic virial coefficients may readily be treated together with spectroscopic data in such a 'direct-potential-fit' (DPF) analysis. Moreover, experimental data for transport properties, such as shear viscosity, thermal conductivity and, to a more limited extent, diffusion and thermal diffusion, may also be utilized for refining potential energy functions for species bound by Van der Waals interactions.

Equation-of-state virial data, in the form of the second virial coefficient, $B_2(T)$, hereinafter referred to as the "pressure" virial coefficient, are often available over a fairly extensive temperature range. Values of the pressure virial coefficient are obtained from fits of pressure-volume data to the virial equation

$$\frac{P\overline{V}}{RT} = 1 + B_2(T)\,\overline{\rho} + B_3(T)\,\overline{\rho}^2 + \cdots \,, \tag{2}$$

in which P is pressure, $\overline{V}$ is molar volume and $\overline{\rho}$ its reciprocal, R is the universal gas constant, T is the temperature, and $B_2(T)$, $B_3(T)$, $\cdots$, are the pressure virial coefficients. We shall be concerned here solely with the second virial coefficient, $B_2(T)$, as it depends only upon the two-body interaction.

At sufficiently high temperatures, classical mechanical values for second virial coefficients may be computed with an accuracy that is better than the experimental uncertainty. At lower temperatures, however, quantum mechanical corrections may become important enough to require their inclusion. Except for gaseous He at all temperatures, and for Ne at very low temperatures, it suffices to add the semi-classical Wigner-Kirkwood corrections, which leads to the expansion [66]

$$B_2(T) = B_{2,\mathrm{cl}}(T) + \left(\frac{\hbar^2}{2\mu}\right) B^{(1)}_{2,\mathrm{qm}}(T) + \left(\frac{\hbar^2}{2\mu}\right)^2 B^{(2)}_{2,\mathrm{qm}}(T) + \cdots \quad , \tag{3}$$

with $\hbar$ the Planck constant divided by 2π, and μ the reduced mass of the interacting pair. The term $B_{2,\mathrm{cl}}(T)$ is the classical contribution, while $B^{(1)}_{2,\mathrm{qm}}(T)$ and $B^{(2)}_{2,\mathrm{qm}}(T)$ are the first and second

quantum corrections, respectively. These quantities are given by

$$B_{2,\mathrm{cl}}(T) = -2\pi N_0 \int_0^\infty \left[\mathrm{e}^{-\beta V(r)} - 1\right] r^2 \, \mathrm{d}r \quad , \tag{4}$$

$$B^{(1)}_{2,\mathrm{qm}}(T) = 2\pi N_0 \beta \int_0^\infty [\beta V'(r)]^2 \mathrm{e}^{-\beta V(r)} r^2 \, \mathrm{d}r \quad , \tag{5}$$

and

$$B^{(2)}_{2,\mathrm{qm}}(T) = -\frac{\pi N_0 \beta^2}{6} \int_0^\infty \left\{ \tfrac{1}{10}[\beta V''(r)]^2 + \tfrac{1}{5r^2}[\beta V'(r)]^2 + \tfrac{1}{9r}[\beta V'(r)]^3 - \tfrac{1}{72}[\beta V'(r)]^4 \right\} \mathrm{e}^{-\beta V(r)} r^2 \, \mathrm{d}r \quad , \tag{6}$$

in which $V'(r)$ and $V''(r)$, respectively, are the first and second radial derivatives of the potential energy function. Straightforward applications of calculus readily yield the analogous integral expressions for the partial derivatives with respect to potential function parameters, $\partial B_2(T;\{p_i\})/\partial p_j$, that are required for incorporating this property into a least-squares-fit procedure. Note that although third quantum corrections to the pressure virial coefficients are not difficult to compute, their contributions are typically much smaller than the experimental uncertainties at all temperatures for which argon pressure virial coefficient data are available: for this reason, they have been neglected.

While spectroscopic data relate directly to the interaction energy (pair-potential) in that each spectroscopic transition energy (1) is determined by the difference between the eigenenergies of the initial and final molecular states, virial coefficient data are encumbered by a layer of averaging that involves a thermally-weighted integration over all possible interatomic separations. This averaging makes the virial data inherently less sensitive to the detailed shape of the potential energy function. Moreover, pressure virial coefficient measurements typically have experimental uncertainties of the order of 1%, and are thus relatively less precisely determined than spectroscopic transition frequencies. These disadvantages are nonetheless partially countered by the ability to obtain virial coefficient data over extensive temperature ranges (of order 100 K to 3000 K), thereby enhancing their overall sensitivity to the nature of the short-range repulsive wall.

Due to relatively recent improvements in acoustic resonators, adiabatic speed-of-sound measurements can now be carried out much more accurately than equation-of-state pressure-volume measurements, with experimental uncertainties typically of order 0.1%. Speed-of-sound data may be represented by a virial equation having a form [67, 68] similar to that of Eq. (2), namely,

$$u^2_{\mathrm{ad}}(T,\overline{\rho}) = \frac{RT\gamma^\circ}{\overline{M}} \left[1 + \beta_{2\mathrm{a}}(T)\,\overline{\rho} + \beta_{3\mathrm{a}}(T)\,\overline{\rho}^2 + \cdots\right] \quad , \tag{7}$$

in which u_{ad} is the adiabatic speed of sound, γ° is the ideal gas value of the heat capacity ratio $\gamma \equiv C_P/C_V = 5/3$, $\overline{M}$ is the molecular weight, $(RT\gamma^\circ/\overline{M})^{\frac{1}{2}} = u^\circ_{\mathrm{ad}}$ is the adiabatic speed of sound for an ideal gas, while $\beta_{2\mathrm{a}}(T)$ and $\beta_{3\mathrm{a}}(T)$ are the second and third acoustic virial coefficients, respectively. We shall be concerned here only with $\beta_{2\mathrm{a}}(T)$, which is related to the second pressure

virial coefficient $B_2(T)$ and its first and second derivatives with respect to temperature by [67–69]

$$\beta_{2a}(T) = 2B_2(T) + 2(\gamma^\circ - 1)\, T\, \frac{\mathrm{d}B_2}{\mathrm{d}T} + \frac{(\gamma^\circ - 1)^2}{\gamma^\circ}\, T^2\, \frac{\mathrm{d}^2 B_2}{\mathrm{d}T^2} \quad . \tag{8}$$

Integral expressions for classical and quantum correction contributions to $\beta_{2a}(T)$ and their partial derivatives with respect to potential function parameters may be obtained readily from Eqs. (3)-(6) and (8).

In the 1960-70's great hopes were placed on the possible use of atomic/molecular beam scattering measurements as a source of information on interatomic and intermolecular potentials. Unfortunately, almost all scattering measurements for rare gas pairs were carried out for collision energies in the range 50 $\mathrm{cm}^{-1} \leq E_{\mathrm{scatt}} \leq 800\ \mathrm{cm}^{-1}$ that is already adequately covered by available pressure and acoustic second virial coefficient data. Moreover, for most differential scattering cross section measurements, comparisons between experimental and calculated results are hampered by a requirement for averaging over a set of experimental conditions that often were not specified explicitly in the literature. In such cases, comparisons could only be carried out by utilizing centre-of-mass scattering pseudo-data generated from the (relatively crude) PEF that had been reported in the original experimental work, a distinctly unsatisfying procedure.

The only reported experimental data that depend almost exclusively on short-range repulsive rare gas atom interactions are a set of very high-energy atomic beam total integral scattering cross section measurements carried out by Rol and co-workers during the early 1970s. They obtained results for all possible noble gas pairs and fitted them to the short-range analytic form $V(r) = A\,\mathrm{e}^{-\alpha r}$ for particular ranges $r \in [r_{\mathrm{min}}, r_{\mathrm{max}}]$. Values of A, α, r_{min} and r_{max} for the He–He system were reported in Ref. [70], while analogous parameter sets for the other fourteen high energy atom–atom interactions were communicated to R. A. Aziz, and cited by him in a major review paper in 1984 [71]. A set of ten short-range interaction energy pseudo-data generated from those Ar–Ar parameters were also employed by Aziz [57] as part of the data set utilized to determine his HFD-ID PEF for Ar_2.

In the present work, spectroscopic data, equation-of-state pressure virial coefficients, and acoustic second virial coefficient data are treated as 'primary' data for optimizing the parameters that define the PEF for the ground state of Ar_2. Both $B_2(T)$ and $\beta_{2a}(T)$ probe the interaction potential energy in much the same fashion. However, as speed-of-sound measurements normally can be made much more accurately than equation-of-state pressure-volume measurements, acoustic virial coefficient values extracted from them are also considerably more accurate than pressure-volume virial coefficient values (typically of the order of $\pm 0.1\,\%$ vs. $\pm 1\,\%$).

Transport properties such as viscosity, thermal conductivity and diffusion coefficients also depend on thermal averages of the PEF over all distances. and hence may be expected to provide insight regarding the nature of the short-range potential wall. However, their simulation is encumbered by *three* layers of integration, over atomic pair-separation, impact parameter, and relative kinetic energy of colliding atom pairs. They are also subject to experimental accuracy/precision problems. Consequently, they are treated as 'secondary' data in the present analysis, in that they are utilized

primarily to test the predictive power of the PEF determined from a fit to the primary data and in a manual (as opposed to automated) fit to refine the final recommended PEF.

The empirical analysis reported in the present work was carried out using program **dPotFit** of Ref. [72], which performs non-linear least-squares fits that employ the exact partial derivatives of the observables with respect to the PEF parameters, p_j, to predict parameter changes from one fit-cycle to the next, until a specified degree of convergence has been attained. The quality of a multiparameter fit of a PEF to a set (or sets) of data is typically characterized by the value of the dimensionless root-mean-square deviation (DRMSD, or $\overline{dd}$) between calculated, $y_{\rm calc}(i)$, and experimental, $y_{\rm obs}(i)$, values for the input data. This quantity, denoted herein by $\overline{dd}$, is defined as

$$\overline{dd} \equiv \sqrt{\frac{1}{N_{\rm dat}} \sum_{i=1}^{N_{\rm dat}} \left(\frac{y_{\rm calc}(i) - y_{\rm obs}(i)}{u_i} \right)^2} \; , \tag{9}$$

in which $N_{\rm dat}$ is the number of data fitted and u_i is the experimental uncertainty associated with datum i. The quality of agreement for any particular subset of data may be computed in the same manner. As a result, if data subsets are labelled by 'α', then the overall $\overline{dd}$ value is related to the subset values $\overline{dd}_\alpha$ by

$$\overline{dd}_{\rm tot} \; \equiv \; \overline{dd} \; = \; \left[\frac{1}{N_{\rm dat}} \sum_\alpha N_{\rm dat}(\alpha) \, (\overline{dd}_\alpha)^2 \right]^{\frac{1}{2}} \; ,$$

with $N_{\rm dat}(\alpha)$ the number of data of type α, and $N_{\rm dat} = \sum_\alpha N_{\rm dat}(\alpha)$.

3. Models for The Potential Energy Function

The traditional three-parameter Morse [6] potential energy function, $V_{\rm M}(r)$, for the interaction energy between two chemical species separated by a distance r may be written as

$$V_{\rm M}(r) \; = \mathfrak{D}_{\rm e} \left[1 - {\rm e}^{-\beta(r - r_{\rm e})} \right]^2 \; , \tag{10}$$

in which parameters $r_{\rm e}$ and $\mathfrak{D}_{\rm e}$ specify the location and strength of the pair interaction energy at the minimum that characterizes equilibrium, while the third parameter, β, together with $\mathfrak{D}_{\rm e}$, determines the curvature of $V_{\rm M}(r)$ at $r_{\rm e}$. The Morse PEF was employed by spectroscopists to represent interaction potential energies of diatomic molecular species for more than fifty years. During much of this same period, interaction PEFs extracted from analyses of the temperature dependence of macroscopic properties, such as the second virial coefficient and transport coefficients, were represented mainly by Lennard-Jones PEFs. This dichotomy led to the practise of referring to diatomic PEFs extracted from molecular spectroscopic data as "*intra*molecular" and to those extracted from macroscopic (bulk) property data as "*inter*molecular".

Extensions of the Morse diatomic PEF were motivated by the realization that atomic interaction energies could be determined to spectroscopic accuracy by fully quantum mechanical direct non-linear least-squares fits of all available spectroscopic data to multiparameter algebraic functions [73–75]. This contrasted strongly with the traditional route of defining the potential energy function

by sets of turning point pairs obtained by applying the semi-classical RKR procedure to empirical analytic expressions for the vibrational energies and inertial rotational constants. An initial effort in this direction, but still utilizing semiclassical RKR turning points, was the introduction of the 'generalized Morse oscillator' (GMO) PEF by Coxon and Hajigeorgiou [76]. However, as the GMO functional form often extrapolates poorly [77], Lee *et al.* [78] introduced the 'expanded Morse oscillator' (EMO) PEF, an analogous form that provides stable extrapolation to large and small distances, and hence is capable of yielding realistic predictions for the energies of high vibrational and/or rotational levels. The EMO PEF (see also Ref. [26]) has the form

$$V_{\rm EMO}(r) \equiv \mathfrak{D}_{\rm e} \left[1 - {\rm e}^{-\beta_{\rm EMO}(r)(r-r_{\rm e})}\right]^2 \quad , \tag{11}$$

with an exponent-coefficient 'shape' function $\beta_{\rm EMO}(r)$ represented by a polynomial expansion

$$\beta_{\rm EMO}(r) = \sum_{i=0}^{N_\beta} \beta_i \left[y_q^{\rm ref}(r)\right]^i \tag{12}$$

in powers of a generalized Šurkus variable [21] $y_q^{\rm ref}(r)$ defined as

$$y_q^{\rm ref}(r) \;\equiv\; \frac{r^q - {r_{\rm ref}}^q}{r^q + {r_{\rm ref}}^q} \quad , \tag{13}$$

with the values of q and of the location of the expansion centre $r_{\rm ref}$ being selected manually.

Somewhat later, the 'Morse-long-range' (MLR) function, a fully analytic PEF that explicitly incorporates realistic long-range behaviour, was introduced by Le Roy and Henderson [23]. In its more general current form it may be written as [25, 26]

$$V_{\rm MLR}(r) \;\equiv\; \mathfrak{D}_{\rm e} \left[1 - \frac{u_{\rm LR}(r)}{u_{\rm LR}(r_{\rm e})}\, {\rm e}^{-\beta_{\rm MLR}(r)\, y_p^{\rm eq}(r)}\right]^2 \quad . \tag{14}$$

This function may be thought of as a generalization of the original three-parameter Morse [6] PEF of Eq. (10) in which the introduction of the exponential prefactor, the use of a dimensionless radial variable $y_p^{\rm eq}(r)$, and the imposition of a fixed limiting-long-range value for the exponent function $\beta_{\rm MLR}(r)\, y_p^{\rm eq}(r)$ combine to constrain its limiting long-range behaviour to have a specified form, $u_{\rm LR}(r)$. MLR functions are everywhere continuous and differentiable to all orders, and can incorporate any plausible form for $u_{\rm LR}(r)$ [24, 31].

The dimensionless radial variable $y_p^{\rm eq}(r)$ appearing in Eq. (14) has the same form as the expansion variable of Eq. (13), but with the integer q replaced by p, and with the reference distance $r_{\rm ref}$ replaced by the equilibrium distance $r_{\rm e}$. It plays the same role in $V_{\rm MLR}(r)$ that the difference $(r - r_{\rm e})$ plays in the Morse PEF, except that $y_p^{\rm eq}(r)$ approaches 1 (rather than ∞) for very large separations.

Similarly, the slowly-varying exponent-coefficient shape function,

$$\beta_{\rm MLR}(r) \;\equiv\; \beta_\infty\, y_p^{\rm ref}(r) + [1 - y_p^{\rm ref}(r)] \sum_{i=0}^{N_\beta} \beta_i [y_q^{\rm ref}(r)]^i \quad , \tag{15}$$

is a generalization of the shape parameter $\beta_{\rm EMO}(r)$ of Eq. (12) that is constrained to approach a limiting value, β_∞, at very large r. The dimensionless polynomial expansion variable again has the form of Eq. (13), while the 'switching function' variable $y_p^{\rm ref}(r)$ has that same form, but with the integer q replaced by the same integer p used to define the dimensionless distance variable $y_p^{\rm eq}(r)$.

The constraint that causes $V_{\rm MLR}(r)$ to assume the desired long-range form

$$V_{\rm MLR}(r) \sim \mathfrak{D}_{\rm e} - u_{\rm LR}(r) + \frac{1}{\mathfrak{D}_{\rm e}}\,[u_{\rm LR}(r)]^2 \tag{16}$$

is the requirement that the limiting long-range value of $\beta_{\rm MLR}(r)$, and hence also of the overall exponent function $\beta_{\rm MLR}(r)\, y_p^{\rm eq}(r)$, be defined as

$$\beta_\infty = \ln\left[\frac{2\,\mathfrak{D}_{\rm e}}{u_{\rm LR}(r_{\rm e})}\right]. \tag{17}$$

The shape function $\beta_{\rm MLR}(r)$ is thus defined in terms of a set of $N_\beta + 1$ empirical shape parameters β_i $(i = 0, 1, \cdots, N_\beta)$, the reference separation $r_{\rm ref}$, and the (small, positive) integers p and q.

The long-range function $u_{\rm LR}(r)$ that defines the exponential prefactor in the MLR function of Eq. (14) is normally written as a sum of individually-damped inverse-power terms, namely,

$$u_{\rm LR}(r) \;\equiv\; \sum_{m=m_{\rm min}}^{m_{\rm max}} D_m^{(s)}(r)\,\frac{C_m}{r^m} \quad . \tag{18}$$

The damping functions $D_m^{(s)}(r)$ used herein are generalized [25] Douketis-Scoles-type [8] damping functions whose form causes $V_{\rm MLR}(r)$ to behave as r^{2s} for very small r. Rather than setting $s = -1$, as was suggested in Ref. [25], the value $s = -1/2$ is employed in the present work, as it gives a Coulombic r^{-1} PEF behaviour at ultra-short separations. Values for $m_{\rm min}$, for the inverse-powers of the leading long-range interaction terms, and for the associated dispersion and/or induction coefficients themselves, depend upon the specific natures of the interacting atoms. Choice of the value for $m_{\rm max}$ is, however, somewhat more subjective.

The MLR functional form thus involves a total of $N_\beta + N_{\rm LR} + 7$ free parameters: in addition to the $N_\beta + 4$ parameters ($r_{\rm ref}$, q, $\{\beta_i | i = 0, \cdots, N_\beta\}$, and N_β) that appear in the shape function $\beta(r)$, there are $N_{\rm LR}$ long-range dispersion/induction coefficients, the equilibrium separation, $r_{\rm e}$, and well-depth, $\mathfrak{D}_{\rm e}$, defining the minimum in the PEF, plus the power p determining the specific form for the dimensionless radial switching function $y_p^{\rm eq}(r)$. However, only $r_{\rm e}$, $\mathfrak{D}_{\rm e}$ and the $N_\beta + 1$ exponent expansion parameters $\{\beta_i | i = 0, \cdots, N_\beta\}$ are varied freely in the present least-squares fitting procedure, while the power q and expansion centre $r_{\rm ref}$ were optimized manually, and the

power p is constrained to be greater than $m_{\max} - m_{\min}$ so that the leading long-range contribution from the exponential factor in $V_{\rm MLR}(r)$, which is proportional to $1/r^{m_{\min}+p}$, will not modify the long-range interaction energy from the specified form, $u_{\rm LR}(r)$ [23]. Because reliable theoretical values for the C_m coefficients are often available from the literature most, if not all, of the relevant C_m values may normally be fixed at predetermined values in the MLR model.

4. Determination of the $Ar_2(X\,^1\Sigma_g^+)$ Potential Energy Function

4.1 Experimental Data for Gaseous Argon.

The first discrete spectra obtained for a ground-state rare-gas pair were the band heads for nine electronic band systems of Ar_2 reported by Tanaka and Yoshino [34] in 1970. These results yielded estimates of the spacings $\Delta G_{v+1/2}$ for the five lowest vibrational levels, and analysis of the associated four vibrational level spacings yielded estimates of the ground-state dissociation energy, $\mathfrak{D}_0$ and well depth $\mathfrak{D}_{\rm e}$, and the leading vibrational constants ω_e and $\omega_e x_e$ [34, 35]. Six years later, a re-examination of one of the band systems at higher resolution enabled Colbourn and Douglas [36] to carry out an analysis that yielded rotational constants and improved values for the spacings amongst the first six vibrational levels, which in turn led to an RKR-based pointwise potential function. Finally, a decade later Herman et al. [37] used tunable coherent VUV radiation produced with four-wave-sum mixing in a nonlinear medium to excite fluorescence from cold ($\sim 40\,$K) Ar_2 dimers formed in a supersonic beam expansion of argon gas. Their results had slightly higher precision than those of Colbourn and Douglas [36], and their 1397 reported transition energies comprise the spectroscopic data used in the present work (see the first segment of Table 1).

The earliest determinations of virial coefficients from equation-of-state isotherm data for argon were reported over a century ago. Since that time, equation-of-state data have been collected in numerous laboratories and analyzed to extract second, $B_2(T)$, and third, $B_3(T)$, virial coefficients from them. Such virial data obtained for argon prior to 1998 have been summarized in the critical compilation of Dymond et al. [91]. For convenience, we shall henceforward refer to virial coefficients determined from equation-of-state data as "pressure" virial coefficients.

We have chosen to include only pressure second virial coefficient values that have been determined after 1940 and with precisions better than 1%. The sources and temperature ranges for the 178 data thereby selected for the determination of a new empirical argon (MLR) PEF have been summarized in the second segment of Table 1. The equation-of-state data of Michels et al. [79, 80] and of Gilgen et al. [84] have been re-fitted using a nonlinear least-squares procedure to obtain values of $B_2(T)$ with uncertainties that take into account all uncertainties in the experimental data and statistical uncertainties introduced through model dependence. Similarly, the equation-of-state data of Klimeck et al. [86] and the compressibility values generated by Estrada-Alexanders and Trusler [85] from speed-of-sound data have been analyzed using the same procedure to generate values of the second pressure virial coefficient plus corresponding uncertainties.

Reliable and accurate measurements of the speed of sound in argon as a function of temperature and density have become available during the past thirty years. Nonlinear least-squares fits to a virial expansion of such speed-of-sound data have enabled the extraction of second acoustic virial

Table 1. Primary Experimental Data

			literature source		
data type	#data	data range	unc.[a]	lead author (year)	Ref.
UV spec. $A\,1_u \rightarrow X\,0_g^+$	456	$v' = 24\text{-}30, v'' = 0\text{-}1$	$0.04 - 0.08$	Herman (1988)	[37]
UV Spec. $B\,0_u^+ \rightarrow X\,0_g^+$	780	$v' = 20\text{-}27, v'' = 0\text{-}5$	$0.07 - 0.14$	Herman (1988)	[37]
UV Spec. $C\,0_u^+ \rightarrow X\,0_g^+$	161	$v' = 0\text{-}4, v'' = 0\text{-}3$	$0.05 - 0.10$	Herman (1988)	[37]
pressure virial	7	$273 - 424\,\mathrm{K}$	0.16-0.63	Michels[b] (1949)	[79]
coefficients	12	$133 - 249\,\mathrm{K}$	0.14-0.76	Michels[b] (1958)	[80]
	18	$84 - 271\,\mathrm{K}$	$1.0 - 4.0$	Byrne (1968)	[81]
	28	$100 - 3273\,\mathrm{K}$	1.0	Kestin (1984)	[82]
	18	$81 - 3000\,\mathrm{K}$	$0.5 - 5.0$	Sevast'yanov (1987)	[83]
	14	$75 - 700\,\mathrm{K}$	$0.1 - 1.0$	Ewing (1992)	[47]
	26	$110 - 340\,\mathrm{K}$	$0.25 - 1.3$	Gilgen[b] (1994)	[84]
	34	$110 - 450\,\mathrm{K}$	$0.1 - 0.5$	Estrada-Alexanders[b] (1996)	[85]
	13	$235 - 520\,\mathrm{K}$	$0.02 - 0.25$	Klimeck[b] (1998)	[86]
	8	$234 - 505\,\mathrm{K}$	$0.1 - 0.6$	Cencek (2013)	[87]
acoustic virial	2	$273 - 303\,\mathrm{K}$	$0.008 - 0.015$	Moldover (1988)	[45]
coefficients	9	$100 - 304\,\mathrm{K}$	$0.03 - 0.09$	Ewing (1989)	[46]
	4	$255 - 300\,\mathrm{K}$	$0.009 - 0.023$	Ewing (1992)	[88]
	8	$90 - 373\,\mathrm{K}$	$0.06 - 0.14$	Ewing (1992)	[47]
	21	$110 - 450\,\mathrm{K}$	$0.04 - 0.10$	Estrada-Alexanders (1995)	[89]
	6	$217 - 303\,\mathrm{K}$	$0.016 - 0.028$	Moldover (1999)	[54]
	9	$234 - 363\,\mathrm{K}$	$0.021 - 0.036$	Benedetto (2004)	[90]

[a] Uncertainties in units [cm^{-1}] for VUV transitions (rows 1–3), and [cm^3/mole] (rows 4–end) for second virial coefficients.

[b] Equation-of-state pressure virial coefficients determined as explained in the text.

coefficients, $\beta_{2a}(T)$, with small statistical uncertainties. The sources and temperature ranges for speed-of-sound data and the 59 values for the second acoustic virial coefficient obtained from these data are summarized in the third segment of Table 1. Indeed, the uncertainty ranges presented in Table 1 for the two types of virial coefficient clearly demonstrate typical differences in precision.

The data described in Table 1 are the 'primary data' that may be employed for DPF analyses using the current version of program **dPotFit**. In addition, however, transport property measurements, especially those made at elevated temperatures, are also sensitive to the nature of

the repulsive wall at distances r shorter than the separation σ at which $V(r)$ changes sign. Although transport property data cannot presently be utilized directly in **dPotFit**, they have been employed in 'forward' calculations to test the various PEFs and to 'tune' and improve the PEF being determined in the final stage of the present analysis. Three classes of experimental results are contained in the transport property data set. The first data class consists of sets of independent measurements, and comprises 252 viscosity, 99 thermal conductivity, 26 self-diffusion, and 45 thermal diffusion data. The second data class consists of a set of 22 *relative* viscosity and 11 *relative* self-diffusion values, defined by the measurement of the ratio of a value of this property relative to a specified reference value. The third data class consists of values obtained via smoothed fits to previously-obtained experimental data: specifically, the data analyzed in Ref. [82] (values of η, λ, $D_{A'A}$, α_0 for 29 temperatures, $80\,\mathrm{K} \leq T \leq 3273\,\mathrm{K}$), Ref. [92] (values of λ for 54 temperatures, $80\,\mathrm{K} \leq T \leq 2000\,\mathrm{K}$), and Ref. [93] (values of λ for 13 temperatures, $200\,\mathrm{K} \leq T \leq 500\,\mathrm{K}$) make up this class. The overall set of 609 transport coefficient data employed in this way, and consisting of 274 values for the (shear) viscosity coefficient, η, 195 values for the thermal conductivity coefficient, λ, 66 values of the self-diffusion coefficient, $D_{\mathrm{A'A}}$, and 74 values for the reduced thermal diffusion coefficient, α_0, is summarized and sourced in Table 2.

Table 2. Secondary Experimental (Transport) Data

data type	#data	temperature range /K	% unc	literature source Lead Author (year)	Ref.
Viscosity	27	80 – 300	1.0	Johnston (1942)	[94]
	4	223 – 373	0.5	Flynn (1963)	[95]
	2	293, 303	0.8	Kestin (1964)	[96]
	12	114 – 375	1.0	Clarke (1968)	[97]
	3	173 – 298	0.5	Gracki (1969)	[98]
	22	283 – 2100	0.4	Guevera (1969)	[99]
	15	293 – 1600	0.5	Dawe (1970)	[100]
	18	202 – 394	0.084	May (2007)	[101]
	8	298 – 973	0.5	Kestin (1972)	[48]
	8	298 – 973	0.7	Hellemans (1974)	[102]
	9	321 – 1300	1.0	Clifford (1975)	[103]
	9	500 – 6000	3.5	Vargaftik (1984)	[104]
	29	50 – 3273	1.0	Kestin (1984)	[82]
	81	291 – 682	0.2	Vogel (2010)	[105]
	3	298 – 423	0.5	Wilhelm (2000)	[106]
	8	233 – 523	0.5	Evers (2002)	[107]
	1	298.15	0.003	Berg (2012)	[108]
	1	298.15	0.003	Berg (2013)	[109]
	14	298 – 653	0.062	Lin (2014)	[110]
Thermal Conductivity	4	800 – 2000	1.5	Faubert (1972)	[111]
	8	328 – 468	0.5	Haarman (1973)	[112]
	9	900 – 2500	1.5	Springer (1973)	[113]
	13	350 – 2500	1.5	Chen (1975)	[114]
	1	300.65	0.5	Fleeter (1981)	[115]
	3	313 – 375	0.5	Clifford (1981)	[116]
	54	80 – 2000	1.0	Ziebland (1981)	[92]
	1	318.15	0.5	Kestin (1982)	[117]
	5	308 – 429	0.4	Haran (1983)	[118]
	29	50 – 3273	1.5	Kestin (1984)	[82]
	5	313 – 470	0.5	Johns (1986)	[119]
	5	174 – 429	0.8	Mardolcar (1986)	[120]
	13	200 – 500	1.5	Younglove (1986)	[93]
	4	308 – 428	0.5	Millat (1987)	[121]
	5	303 – 463	1.0	Hemminger (1987)	[122]
	12	103 – 324	2.0	Perkins (1991)	[53]
	3	300 – 340	2.0	Roder (2000)	[123]
	3	300 – 340	2.0	Sun (2005)	[124]
	18	203 – 394	0.1	May (2007)	[101]
Thermal Diffusion	6	129 – 720	10.0	Stier (1942)	[125]
	6	233 – 630	5.0	Moran (1958)	[126]
	15	127 – 653	10.0	Paul (1963)	[127]
	7	104 – 287	10.0	Stevens (1968)	[128]
	7	273 – 873	12.5	Taylor (1973)	[129]
	3	338 – 438	5.0	Rutherford (1973)	[130]
	1	215	5.0	Taylor (1975)	[131]
	29	50 – 3273	10.0	Kestin (1984)	[82]
Isotopic Diffusion	7	78 – 353	1.5	Winn (1950)	[132]
	19	77 – 294	3.0	De Paz (1967)	[133]
	11	235 – 418	0.1	Vugts (1969)	[134]
	29	50 – 3273	1.5	Kestin (1984)	[82]

4.2 Parameters to be Fixed or Varied in the MLR model

Of the $N_\beta + N_{\rm LR} + 7$ fit-parameters that define the MLR functional form, the $N_{\rm LR} + 1$ parameters corresponding to the values of the long-range C_m coefficients and of the integer power p are predetermined by the form chosen for the long-range interaction energy $u_{\rm LR}(r)$. In particular, $m_{\rm min} = 6$ because the long-range interaction of a pair of neutral closed-shell atoms is governed entirely by dispersion interactions. As reliable values for the three leading dispersion coefficients for Ar are available from the literature [135, 136] (see Table 5, below), we chose to set $N_{\rm LR} = 3$ and fix the values for C_6, C_8, and C_{10} at literature values. Moreover, as the (integer) power p appearing in $y_p^{\rm eq}(r)$ must exceed $m_{\rm max} - m_{\rm min} = 4$, for this choice of long-range coefficients, it is reasonable to set $p = 6$ (rather than to the minimal value 5) in order that the power of the leading long-range contribution arising from the exponential term in the MLR form match that of the r^{-12} term expected to arise next in the dispersion energy series. Following the 'recipe' of Douketis *et al.* [8], the damping function range scaling parameter was set at $\rho = 1.10$ and, as mentioned near the end of Section 3, the very-short-range power parameter was fixed at $s = -1/2$.

Of the remaining $N_\beta + 6$ parameters, $\mathfrak{D}_e$, r_e and the $N_\beta + 1$ exponent coefficient PEF 'shape' parameters of the MLR form are optimized automatically, while the exponent polynomial order N_β, the integer parameter q and the reference centre $r_{\rm ref}$ for the $\beta(r)$ expansion are determined manually. Initial values were $N_\beta = 0$ and $q = 3$, and $r_{\rm ref}$ equal to the geometric mean of the turning-points for the highest observed vibrational level ($v = 5$) of Ref. [37], a distance of 4.6 Å. Manual refinement of $r_{\rm ref}$ led to $r_{\rm ref} = 5.3$ Å as an optimal choice for the $X\,^1\Sigma_g^+$ ground electronic state of Ar_2. As changes in q had no significant effect on the quality-of-fit, $q = 3$ has been employed in the remainder of this work.

4.3 Fitting to Spectroscopic Data Alone, and Treatment of Upper State Levels

The fluorescence spectra observed and assigned by Herman *et al.* [37] consisted of transitions involving three excited electronic states. Having settled on the type of PEF to be used to represent ground-state Ar_2, the next question to be addressed is how to treat the upper electronic states. The simplest approach would be to treat all of the upper-state levels as independent term values. For this case, the uppermost segment of Table 3 shows how the quality-of-fit to the data improves as the order of the MLR exponent polynomial increases from $N_\beta = 0$ to 3. As 165 of the 1397 transitions are connected to only a single X-state level, they carry no information about the X-state potential, and hence were omitted from this analysis. The total number of *free* parameters in these fits then consisted of 302 upper-state term values plus the X-state MLR parameters.

Since all of the 1397 data were assigned as members of rotational branches in vibrational bands, following Herman *et al.* [37], it would clearly be appropriate to represent those upper state level energies using a set of band constants for each observed vibrational level of each upper state. When the energies of the rotational sublevels for each vibrational level of each state are represented by the three leading 'mechanical' band constants $\{G_{v'}, B_{v'}, D_{v'}\}$, with the constants for the $A\,1_u$ state extended to include the leading Λ-doubling constant $q_{v'}$, the results appearing in the second segment of Table 3 are obtained. While the number of fitted parameters is reduced by more than

Table 3. Summary of fits to spectroscopic data alone, performed with $X\,^1\Sigma_g^+$ state represented by an MLR PEF. Bold font indicate the selected optimum result for each case.

Stage	#data		$\overline{dd}$ for $A\,1_u$	$\overline{dd}$ for $B\,0_u^+$	$\overline{dd}$ for $C\,0_u^+$	$\overline{dd}$ for total	total # param.
1	1232	N_β^X	Term values for all excimer energy levels				
		0	0.874	1.037	1.060	0.994	305
		1	0.694	0.926	0.892	0.862	306
		2	**0.659**	**0.914**	**0.833**	**0.841**	**307**
		3	0.657	0.915	0.827	0.840	308
2	1397	N_β^X	Band constants for all excimer energy levels				
		0	0.993	1.095	1.021	1.054	70
		1	0.872	0.985	0.886	0.938	71
		2	**0.844**	**0.973**	**0.850**	**0.919**	**72**
		3	0.841	0.973	0.844	0.917	73
3	1397	N_β^C	EMO PEF for $C\,0_u^+$ excimer state, with $N_\beta^X = 2$				
		1	1.358	1.267	9.127	3.332	61
		2	0.845	0.980	1.623	1.036	62
		3	0.842	0.974	1.044	0.942	63
		4	**0.844**	**0.972**	**0.889**	**0.923**	**64**
		5	0.844	0.972	0.886	0.922	65

a factor of four, this approach is accompanied by only about 10% increases in the values of $\overline{dd}$, the 'cost' of imposing realistic physical models on the energy levels of the three upper electronic states.

The two upper segments of Table 3 show that the the quality-of-fit parameter $\overline{dd}$ does not improve significantly upon increasing the X-state exponent polynomial order beyond $N_\beta = 2$. Moreover, most of the β_i coefficients yielded by the $N_\beta = 3$ fits had uncertainties greater than 100%. Thus, we conclude that the highest-order MLR PEF for ground-state Ar_2 that can be determined from the spectroscopic data alone is one for which $N_\beta = 2$.

A final level of sophistication for treating the excimer energy levels would be to represent them as levels of analytic model PEFs. The fact that Herman *et al.* [37] were able to provide absolute vibrational assignments for those upper-state vibrational levels, $v' = 24 - 30$ for the $A\,1_u$ state, $v' = 20 - 27$ for the $B\,0_u^+$ state, and $v' = 0 - 4$ for the $C\,0_u^+$ state, made this a tantalizing possibility. However, it was only partially realized, in that we were able to determine a PEF model for the $C\,0_u^+$ state, but not for the other two. In particular, with the levels of the $X\,0_u^+$ state defined by an $N_\beta^X = 2$ MLR function with $q = 3$, $p = 6$ and $r_{\rm ref} = 5.3$ Å, but its other parameters allowed to vary, the fits were repeated using band constants for the $A\,1_u$ and $B\,0_u^+$, states, but with an EMO PEF used to represent the levels of the $C\,0_u^+$ state. For various values of the exponent polynomial order, the results of fits performed with $q = 6$ and $r_{\rm ref} = r_{\rm e}$ are presented in the bottom segment of Table 3. It is clear that those fits converge for $N_\beta^C = 4$, and that the quality of fit there was essentially identical to that obtained using band constants for the $C\,0_u^+$ state. The parameters defining the

resulting C-state EMO potential are reported in Table 5.

4.4 Fitting to the Full Primary Data Set

A basic starting point for the inclusion of experimental pressure and acoustic virial coefficients and other data in the fitting procedure was a forward calculation of their quality of agreement with predictions generated from the optimum PEF determined from fits to the spectroscopic data alone, namely, that associated with the bold-font results in the middle segment of Table 3. The $\overline{dd}$ values obtained in this way are shown in square brackets in the first column of Table 4. Since an ideal $\overline{dd}$ value for any data set or subset would be a number close to 1, it is clear that this 'spectroscopy-alone' PEF yields poor predictions for the virial coefficients, especially for the higher quality acoustic virial data. As it was partially based on values for data not included in the analysis, the first entry in the fourth row of this table has also been presented in square brackets.

The next step was to re-optimize the $N_\beta^X = 2$ X-state MLR potential parameters while incorporating the virial coefficients in the set of data being fitted to. This yielded the second column of $\overline{dd}$ values shown in Table 4. As inclusion of the virial data caused a significant increase in the $\overline{dd}$ value for the spectroscopic data, the fit was repeated with the exponent polynomial order increased to $N_\beta^X = 3$, which yielded the third column of $\overline{dd}$ values in Table 4. Increasing N_β^X further yielded no further improvements in the $\overline{dd}$ values for the full primary data set. The fact that their $\overline{dd}$ values converge to numbers somewhat larger than 1 implies that the uncertainties used for the two types of virial coefficient data may be somewhat too small.

Table 4. Summary of Overall Fit Results.[a] Numbers without brackets are $\overline{dd}$ values for sets of data included in the fits; those in square brackets were obtained as predictions from a fitted potential.

		$\overline{dd}$ values			
		spec	spec / vir		spec / vir / PP[b]
# data	property	$N_\beta^X = 2$	N_β^X=2	N_β^X=3	N_β^X=4
1397	spectroscopy	0.919	0.948	0.922	0.922
178	pressure virials	[8.273]	1.163	1.141	1.162
59	acoustic virials	[43.661]	2.469	2.309	2.360
1634	all primary data	[8.779]	1.066	1.030	1.036
609	transport data	[1.185]	[1.008]	[1.236]	1.061
2243	All Data	[7.518]	[1.051]	[1.090]	1.043

[a] All MLR PEFs have $r_{\rm ref} = 5.3\,$Å, $p = 6$, $q = 3$, and employ $s = -\frac{1}{2}$ damping functions.

[b] A manually-tuned 'pull-point' (PP) of $V(r = 2.8\,\text{Å}) = 1705$ cm^{-1} was treated as an added datum in the fit.

4.5 Incorporating Transport Property Data into the Analysis

While they cannot be treated as experimental data in DPF program **dPotFit**, transport properties have long been considered to provide a useful test of the accuracy of rare-gas-pair PEFs, particularly in the short-range repulsive wall region. The first three entries on the fifth row of Table 4 therefore list the $\overline{dd}$ values calculated for the 593 transport property data of Table 2 using the three fitted potentials described above. These 'forward' calculations were carried out using a program based upon code listed in Appendix 12 of Ref. [137]. The trend seen there shows that extending the MLR exponent polynomial order to $N_\beta^X = 3$ in order to obtain improved agreement with the virial data yielded a PEF whose predictions for the transport properties were substantially worse (by 20%!). This indicated that a higher-order MLR function would be needed in order to attain good fits to both the primary (spectroscopy and virial coefficients) and secondary (transport property) data. Moreover, as the shape of the PEF in the well region is sharply defined by the spectroscopic data and the theoretically known long-range coefficients, this (mis)behaviour was attributed to a problem with the short-range repulsive wall.

As the final stage of the analysis, a series of fits to all of the primary data were then performed with the repulsive wall constrained to pass through a manually-selected 'pull point' PEF value set at a distance of 2.8 Å, at which the repulsive walls of the first three potentials of Table 4 began to diverge. In particular, a value of $\overline{dd}$ for the transport data was calculated from each of the fitted PEFs obtained as the energy at that 'pull point' was varied, in order to optimize the $\overline{dd}$ value

Table 5. Fitted parameters defining the recomended for MLR potential[a] for ground-state ($X\,^1\Sigma_g^+$) Ar_2 and the EMO PEF[b] for the $C\,0_u^+$ state discussed in subsection 4.3.

	MLR PEF[a] for $X\,^1\Sigma_g^+$	EMO PEF[b] for $C\,0_u^+$
	N_β^X=4	N_β^C=4
parameter	(spec/vir/PP)	(spec)
$r_{\rm ref}$ /Å	5.3	$r_{\rm e}(C\,0_u^+)$
$\mathfrak{D}_{\rm e}$ /cm^{-1}	99.49(4)	465.35(11)
$r_{\rm e}$ /Å	3.766(2)	3.594(2)
β_0	0.04743	1.6704
β_1	0.0877	0.0221
β_2	0.112	−1.211
β_3	0.57	−0.78
β_4	0.33	1.1

[a] Predetermined MLR parameters: $p = 6$, $q = 3$, $C_6 = 3.105 \times 10^5\,{\rm cm}^{-1}{\rm Å}^6$ [135], $C_8 = 2.219 \times 10^6\,{\rm cm}^{-1}{\rm Å}^8$, $C_{10} = 1.899 \times 10^7\,{\rm cm}^{-1}{\rm Å}^{10}$ [136], and $r_{\rm ref} = 5.3$ Å.

[b] Predetermined $q = 6$, and an asymptote energy 95,399.8276 cm^{-1} above that for the ground state [138].

calculated for 'All Data' (row 6 in Table 4). As indicated by the header of the final column in Table 4, retaining good agreement with the primary data while applying this additional constraint required a further increase in the order of the MLR exponent polynomial to $N_\beta^X = 4$. No further improvement in the quality of fit was obtained for $N_\beta^X = 5$.

In a comparison between the $\overline{dd}$ values seen in the last two columns of Table 4, the 2.3% net improvement in $\overline{dd}$ for 'All Data' (row 6) is mainly due to the 17.5% improvement in $\overline{dd}$ for the transport property data (row 5), countered by a very small (0.18%) degradation in the $\overline{dd}$ value for the primary data (row 4). This N_β^X=4 MLR PEF thus provides a statistically significant improvement in the representation of the 2250 experimental data utilized (1657 directly, 593 indirectly) in its determination, and therefore we deem it the new best empirical PEF for ground-state Ar_2. The parameter values defining this recomended MLR PEF for ground-state Ar_2, together with those for the EMO PEF for the $C\,0_u^+$ state associated with the second-last row of Table 3, are presented in Table 5. The numbers in parentheses there are the 95% confidence limit uncertainties in the last digits shown for parameters with explicit physical significance. The compact final form of these parameter values was obtained by application of the sequential rounding and refitting (SRR) procedure of Ref. [139], which minimizes the numbers of significant digits required to describe a fitted data set with no significant loss of precision.

5. Comparisons with Previous PEFs for $Ar_2(X\,^1\Sigma_g^+)$

5.1 Quality-of-fit comparisons

Because of its importance (together with molecular nitrogen) as a primary calibration substance for equation-of-state and transport property measurements, argon has also served as a primary testing ground for the determination of reliable PEFs. It it therefore appropriate to compare the recommended empirical PEF of Table 5 with some of the best previously reported functions. Table 6 compares predictions of the properties of Tables 1 and 2 taken from the last column of Table 4 with predictions generated from two previous empirical PEFs, from two recent high quality *ab initio* PEFs, and from a commonly used semi-empirical analytic function.

The oldest empirical PEF considered here (column 2 of Table 6) was an HFD-type function with individually-damped long-range dispersion contributions that was reported by Aziz [57] in 1993. It was determined primarily via manual fitting to a combination of molecular beam scattering data and second pressure virial coefficient data, together with transport property data and key spectroscopic properties (the inertial B_v constants and vibrational spacings, $\Delta G_{v+\frac{1}{2}}$). Around that time, however, it was realized (see, e.g., Eq.(8) above) that acoustic virial coefficients probe essentially the same regions of the PEF as do pressure virial coefficients, and that speed-of-sound measurements can be made much more precisely than equation-of-state measurements. As second acoustic virial coefficients had not been used in its determination, calculations of their values and their temperature dependence would offer a stringent test of the Aziz PEF. Such a computation was carried out by Boyes [140], who found that the Aziz PEF failed badly in predicting $\beta_{2a}(T)$ values (see row 3 of column 2 of Table 6). Boyes also carried out a redetermination of that HFD-type PEF based upon the input data employed by Aziz, but with the pressure virial coefficient data replaced

Table 6. Dimensionless root-mean-square deviations $\overline{dd}$ between calculated and experimental values of four types of argon data, for six PEF models. $\overline{dd}$ values in square brackets in the first three columns, and *all* $\overline{dd}$ values in last 3 columns, were generated by forward calculations using fixed potential functions.

		$\overline{dd}$					
		Empirical PEFs			*Ab initio* PEFs		TT model
PEF type:		MLR	HFD-ID		TT_{mod}	TT_{mod}	TT
data type	# data	$N_\beta^X = 4$	Aziz[57]	Boyes[140]	[15]	[16]	[141]
spectroscopy	1397	0.922	0.964	0.987	0.938	1.015	3.047
pressure virials	178	1.162	1.764	[1.338]	1.180	1.689	15.759
acoustic virials	59	2.360	[15.253]	2.467	2.442	4.867	114.101
primary data	1634	1.036	3.088	1.117	1.058	1.430	22.474
transport data	609	1.061	2.549	1.142	1.071	1.054	6.454
All Data	2243	1.043	2.951	1.124	1.062	1.337	19.474
$\mathfrak{D}_e$ /cm^{-1}		99.49(4)	99.55	99.54	99.48	99.35	99.64
r_e / Å		3.766(2)	3.757	3.764	3.762	3.762	3.757

by the new acoustic virial data, and a more quantitative treatment of the spectroscopic data. This yielded a new HFD-type PEF that was consistent with acoustic virial and spectroscopic data and, at the same time, gave a much improved level of agreement with the pressure virial and transport property data (see Column 3 of Table 6). However, the present recommended MLR potential (see Column 1 of Table 6) is in distinctly better overall agreement with the data than are either of these older empirical PEFs.

The three final columns of Table 6 then present the results of forward calculations of the properties of Tables 1 and 2 using the recommended analytic representations of the *ab initio* PEFs of Jäger *et al.* [15] and of Patkowski and Szalewicz [16], and the widely cited HFD-type potential of Tang and Toennies [141]. While the 'TT' model of the very last column had the very basic Tang-Toennies-type PEF form, in which the exponent coefficient of the repulsive Born-Mayer term was the same as the scaling parameter in the dispersion damping functions, the modified TT-type functions determined from fits to the *ab initio* points had multiparameter pre-exponential [16] or exponent coefficient [15] factors. The predictions generated from these recent *ab initio*-based PEFs are clearly quite good, the one by Jäger *et al.* yielding a $\overline{dd}$ value for "All Data" only 10% larger that that for our best empirical potential. This result attests to the increasing reliability of high quality *ab initio* calculations for such a large many-electron system.

Results obtained using the two-parameter ($\mathfrak{D}_e$, r_e) TT03 model PEF [141] have been included in Table 6 (last column) primarily to emphasize the fact that no two-parameter PEF, not even one with

accurate long-range coefficients and parameter values ($\mathfrak{D}_e$ and r_e) taken from previous empirical studies, is able to represent the Ar_2 interaction energy well enough to predict actual spectroscopic transition energies, acoustic and pressure second virial coefficients, or transport coefficients close to being within the uncertainties of the experimental values. Of course, this has been well known for simple two-parameter Lennard-Jones and exp-6 model PEFs for many years [41, 42], but it may not have been fully appreciated that this shortcoming also holds for more sophisticated two-parameter model PEFs, even those that include, as does the TT03 model, a sensible representation of the long-range part of the interaction.

5.2 Direct Comparisons Between PEFs

Visual comparisons of the present recommended N_β^X=4 MLR PEF of Table 5 with two precursor best-fit PEFs from the earlier columns of Table 4, namely, the N_β^X=2 MLR PEF fitted to spectroscopic data alone and the N_β^X=3 MLR PEF fitted to spectroscopic and virial data, as well as with the other PEFs of Table 6, are presented in Figs. 1 and 2. While their recommended analytic representations were used to generate the results in the "*Ab Initio* PEF" columns of Table 6, only the *ab initio* points themselves are shown in Fig. 1. It is immediately evident in the lower panel of Fig. 1 that on an energy scale which spans the full well depth, all of these functions become indistinguishable. However, on the logarithmic scale used for the short-range region in the upper panel of Fig. 1 and the expanded-scale view of the potential minimum in Fig. 2, some distinctions become clear.

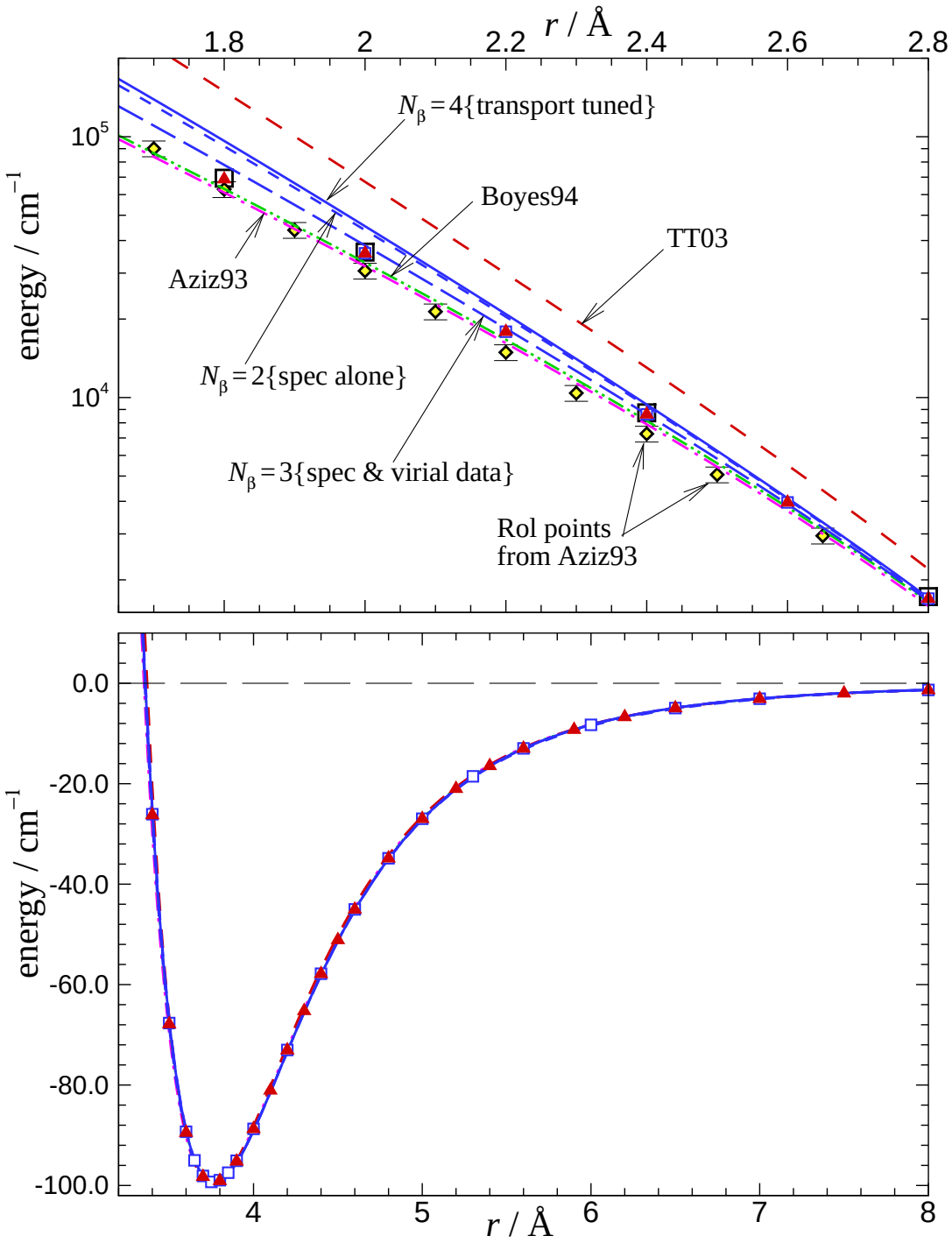

Figure 1. Potential energy functions for the interaction between two ground state argon atoms. Upper panel: short-range (1.7 Å–2.8 Å) behaviour of $V(r)$. Short-dash (blue) curve: N_β=2 MLR PEF (fitted to spectroscopic data alone); long-dash (blue) curve: N_β=3 MLR PEF (fitted to spectroscopic and virial data); solid (blue) curve: N_β=4 MLR PEF (fitted to spectroscopic and virial data, and tuned to transport data); dash-dot (magenta) curve: Aziz [57] PEF; dash-double-dot (green) curve: Boyes [140] PEF; short-dash (red) curve, TT03 model; □ (hollow, black) symbols: ab initio values from Ref. [16]; ▲ (solid, red) symbols: ab initio values from Ref. [15]; ◇ (black, yellow-filled) RoI pseudo-data from Ref. [57]. Lower panel: intermediate-range (3.2 Å–8.0 Å) behaviour of $V(r)$.

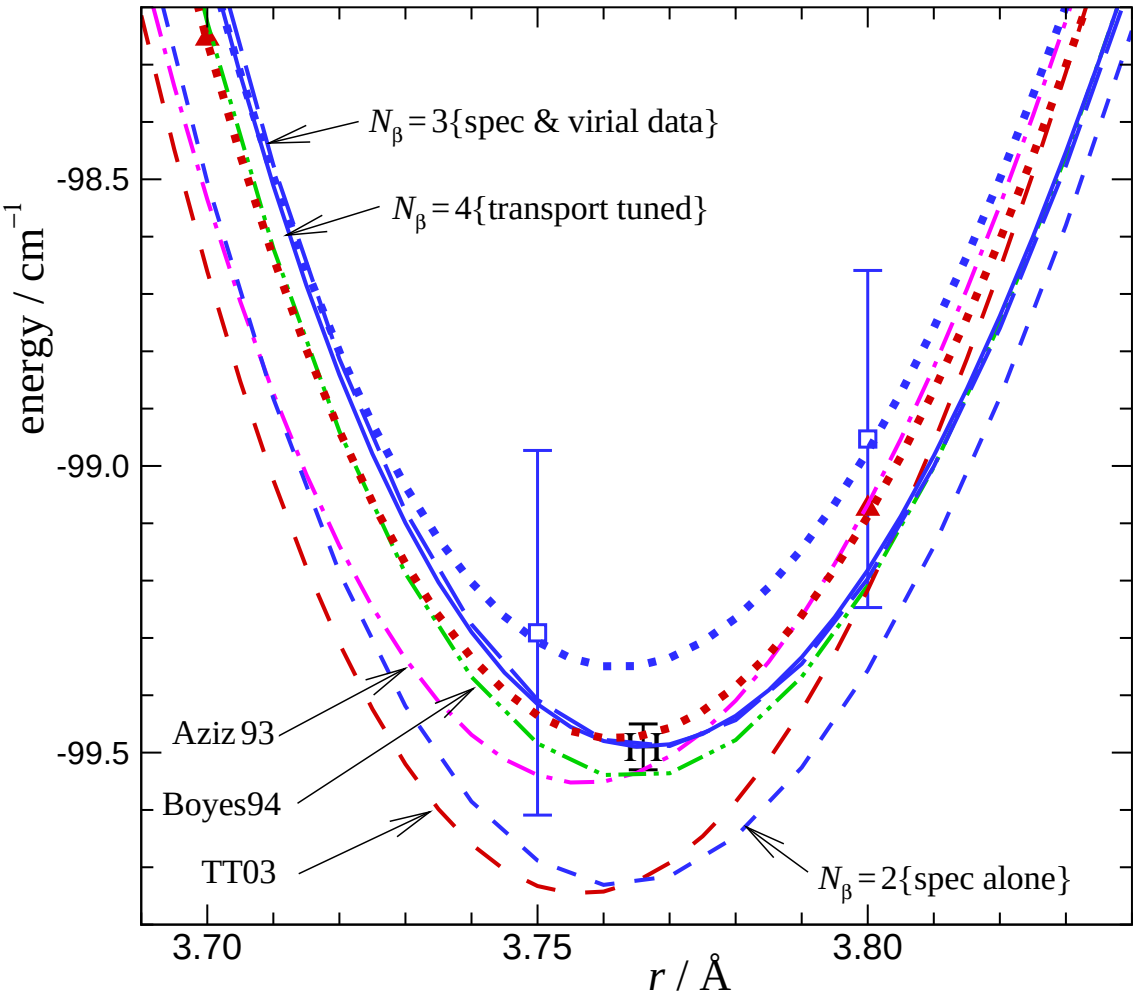

Figure 2. Potential energy functions in the vicinity of the minimum for the $Ar_2(X\,^1\Sigma_g^+)$ ground electronic state interaction energy. Except for the fitted ab initio PEFs from Ref. [15] (red dotted curve and solid triangle points) and Ref. [16] (blue dotted curve and open square points with error bars), the curves and symbols are as identified in the caption for Fig. 1. The minimum, ($\mathfrak{D}_e = 99.50 \pm 0.04\,\mathrm{cm}^{-1}$, $r_e = 3.766 \pm 0.002$ Å), for the recommended best-fit N_β=4 MLR PEF is indicated by the vertical and horizontal error bars.

In particular, most PEFs are distinguishable from one another in the short-range repulsive ($r < \sigma$) region considered in the upper panel of Fig. 1. The three fitted MLR PEFs shown here are: the N_β^X=2 function that was determined from a fit to the spectroscopic data alone (from column 1 of Table 4), the N_β^X=3 MLR function determined from a fit to the full primary data set (column 3 of Table 4), and the recommended N_β^X=4 function obtained by tuning PEFs fitted to the primary data and tuned to yield improved predictions of the transport data (last column of Table 4). As a historical comparison, a set of short-range Ar–Ar interaction energies extracted by Rol and co-workers from molecular beam (MB) measurements of high-energy total integral scattering cross sections (as given in Table II of Ref. [57]) are shown as diamond-shaped points with error bars. However, they systematically lie below both the recent *ab initio* results (solid red triangles and open square points), and from the recommended best empirical PEF (solid blue curve), and are not considered further here.

The five empirical PEFs and the two sets of *ab initio* points are also clearly distinguishable on the expanded scale of Fig. 2, in which the distinct natures of the various PEFs in the vicinity of the the minima of their interaction energies can be seen clearly. Both the *ab initio* points (solid red triangles [15] and open square blue points with error bars [16]) *and* their recommended analytic representations (dotted green and blue curves, respectively) are shown in this figure. Except for the $N_\beta^X = 2$ MLR function determined from spectroscopy alone (short-dash blue curve), the simple Tang-Toennies function [141] (dashed red curve), and the venerable Aziz potential (magenta dash-dot curve), all of these functions have minima lying within the uncertainties of that for our recommended $N_\beta^X = 4$ MLR function (solid blue curve, with black horizontal and vertical error bars at its minimum).

Finally, the ultra-short-range ($r < 1.5$ Å) behaviours of the various PEFs are shown in Fig. 3, together with a number of additional recent *ab initio* points for this region (open square points [65]). The black dotted line on this log-log plot shows the limiting very short-range Coulomb repulsion behaviour of two Ar nuclei with assumed effective charges of +18. All three MLR functions become parallel to this limiting line, by construction, because of the choice of $s = -1/2$ in the definition of their damping functions, while the *ab initio* points appear to be approaching that limiting Coulomb behaviour.

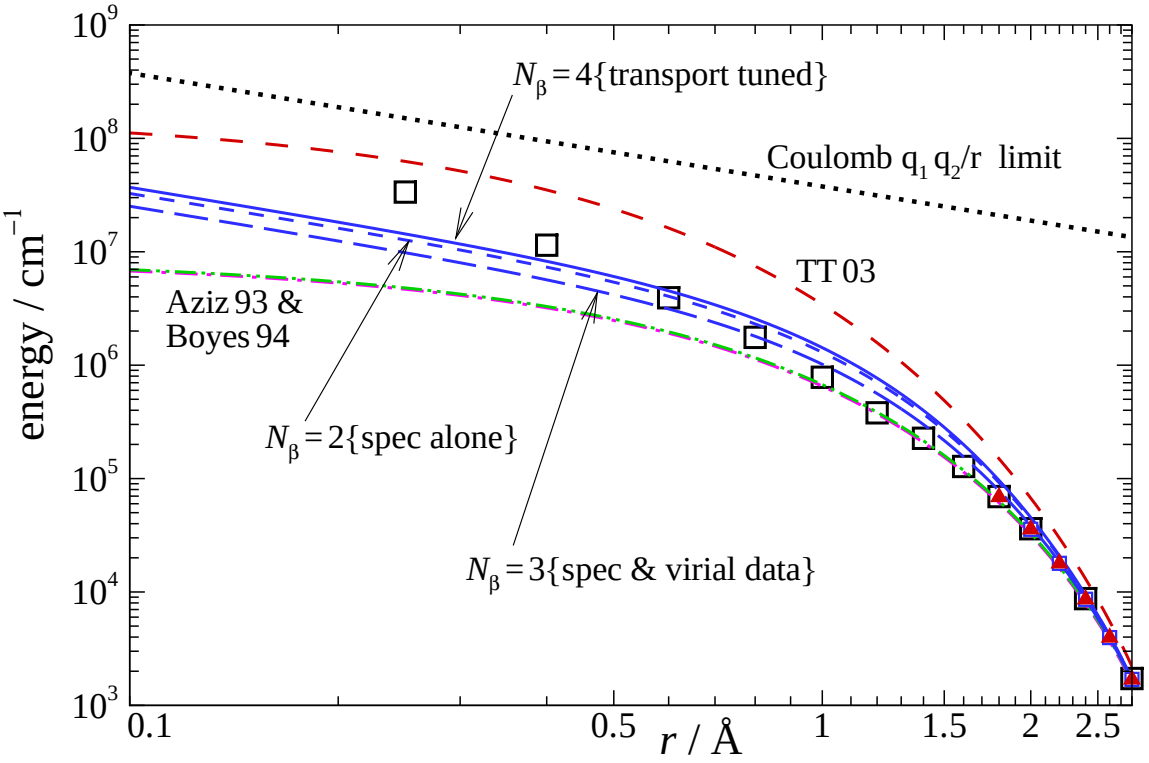

Figure 3. Comparisons between the ultra-short distance (0.1 Å–2.5 Å) behaviours of the empirical N_β=2, 3 and 4 fitted MLR PEFs, the Aziz [57], Boyes [140] HFD-ID empirical fit-PEFs, and the Tang-Toennies two-parameter model for the $Ar_2(X\,^1\Sigma_g^+)$ interaction, as identified in Fig. 1. The Coulomb-limit for the Ar–Ar interaction ($q_1 = q_2 = 18$) is represented by the black dotted line. Symbols: □ (hollow, black) from Ref. [65]; □ (hollow. blue) from Ref. [16]; ▲ (solid, red) from Ref. [15].

Figure 2, taken in conjunction with the lower panel of Fig. 1 and the DRMSD values given in Table 6, makes it clear that the experimental data employed to determine the PEF for the electronic ground-state Ar–Ar interaction potential *are* sensitive to relatively small differences in the well and the repulsive wall for interaction energies less than approximately $1000\,\mathrm{cm}^{-1}$.

6. Discussion and Conclusions

The relative performances of the two recent *ab initio* PEFs [15, 16] in the comparisons of Table 6 is a testament to the excellent quality of current coupled-cluster *ab initio* computational methodology. Note that while Table 6 shows that the *ab initio* PEF of Jäger *et al.* [15] describes neither the primary experimental data set nor the transport data as well as does the empirical N_β=4 MLR PEF, it nonetheless does impressively well, with a $\overline{dd}$ value for "All Data" only 10% larger than that for our best empirical PEF. Moreover, it gives better agreement with all categories of data than does either of the HFD-ID empirical PEFs that had actually been fitted to similar sets of experimental data. It is, however, puzzling that the *ab initio* PEF of Ref. [16] fares much worse in these comparisons than does that of Ref. [15], particularly for the acoustic virial data ($\overline{dd}$ = 4.879 *vs.* 2.479), given that the *ab initio* interaction energies computed in Ref. [15] typically fall within the fairly tight uncertainties assigned to the *ab initio* results reported in Ref. [16].

From qualitative comparisons of the curves shown in Fig. 1, it appears that the largest differences between the *ab initio* results and the various empirical potentials are associated with the relatively few (ten for Ref. [15], seven for Ref. [16]) points obtained at Ar–Ar separations on the repulsive wall (i.e., $r < \sigma$). More quantitative comparisons of the degree of agreement between these two recent high-level *ab initio* calculations [15, 16] and various empirical PEFs are provided by Table 7, for which the $\overline{dd}$ values were obtained by treating the recent higher-level *ab initio* values for the $\mathrm{Ar}_2(X\,^1\Sigma_g^+)$ interaction energies [15, 16] as external data sets, while assuming that the uncertainties reported by Patkowski and Szalewicz [16] could also be used for the results of Jäger *et al.* [15, 142].

The first pair of columns in Table 7 presents the RMS differences across the whole domain, while the second pair of columns give the corresponding $\overline{dd}$-values for the *ab initio* results in the region

Table 7. Comparisons of differences between two sets of *ab initio* points and predictions of various empirical PEFs.

	$\overline{dd}$ {all points}		$\overline{dd}$ {well: $r > \sigma$}		$\overline{dd}$ {wall: $r < \sigma$}	
PEF	Jäger [15]	Patk. [16]	Jäger [15]	Patk. [16]	Jäger [15]	Patk. [16]
N_β=2 MLR	34.10	21.57	4.55	5.13	66.01	45.79
N_β=3 MLR	12.30	6.26	1.97	2.04	23.76	13.00
N_β=4 MLR	41.25	26.00	2.13	2.25	80.34	56.26
Aziz HFD-ID [57]	18.97	13.80	3.90	4.19	36.40	28.85
Boyes HFD-ID [140]	13.42	9.32	1.88	2.19	25.97	16.78
TT(Jäger [15])	0.36	0.74	0.41	0.83	0.11	0.13
TT(Patkowski [16])	0.61	0.30	0.70	0.34	0.17	0.02

of the attractive potential energy well, and the third pair of columns presents the analogous results for the repulsive wall region, $r < \sigma$. It is important to remember that the $\overline{dd}$ values given in Table 7 do not represent tests of the quality of the various potentials, but are simply measures of the level of agreement between the five empirical PEFs and the two sets of *ab initio* points. As might be expected (see last two rows of Table 7), the modified-TT-type PEFs actually fitted to these sets of points by the authors of Refs. [15] and [16] are in much closer agreement with their *ab initio* points in all regions. Note, however, that this is not due to the choice of potential form, as $N_\beta = 3$ MLR PEFs with equivalent numbers of free parameters (i.e., also with C_6 and C_8 free) fitted to those *ab initio* data give overall $\overline{dd}$ values of 0.43 and 0.34, respectively. Finally, the small size of the $\overline{dd}$ value obtained on applying the fitted PEF of Ref. [16] to the *ab initio* points of Ref. [15] and *vice versa* confirms the statement by Patkowski and Szalewicz that the two sets of *ab initio* points agree to within their estimated uncertainties.

In summary, the present work has determined an improved empirical PEF model for the Ar–Ar interaction energy from a combination of a conventional DPF treatment of spectroscopic and second virial coefficient data with a manual 'tuning' of the repulsive wall to incorporate optimization of agreement with transport properties. The resulting function is in distinctly better overall agreement with this body of 2243 data than were the most recent previous empirical potentials (by 7.8% [140] and 182% [57]), or two recent very high quality *ab initio* PEFs (by 1.8% [15] and 28% [16], respectively). We also find that a 2-parameter PEF with a widely used form taken from a highly quoted source [141] ($\gtrsim$ 250 citations to date) has a $\overline{dd}$ value for this data set some 17 times larger than that for the present MLR(N_β=4) empirical PEF. This reaffirms our reservations about the utility of *any* two-parameter model potential form. A comprehensive review of the degree of agreement between predictions generated from the various empirical potentials and the experimental data is presented in the Appendix.

The present empirical MLR PEF also enables the generation of smooth sets of predicted values of the two types of virial coefficients and four types of transport property coefficients considered herein over an extensive temperature range. A compact illustrative version of these results is presented in Table 8: a more extensive tabulation has been included in the Supplemental Data. Such a tabulation should likely supersede the use of fragmentary experimental data sets for the archival representation of our empirical knowledge of these properties.

In contrast with the early near-dissociation theory analysis prediction of Ref. [35], the present recommended MLR potential supports only eight, rather than nine vibrational levels. Note, however, that the prediction of Ref. [35] was based solely upon the low-resolution earliest observations of the vibrational spacings of levels $v = 0 - 4$ [34], and the predicted binding energy for $v = 8$ was, within its uncertainties, $0\,\mathrm{cm}^{-1}$. Finally, we have employed the algorithm of Ref. [143] to compute a value of $-714\,$Å for the ^{40}Ar s-wave scattering length for our recommended PEF. Listings of the binding energies and calculated rotational constants for the eight bound vibrational levels, and of the energies of all 173 truly bound levels and 61 quasibound rotational levels supported by this PEF (together with the tunneling lifetimes of the latter), have been included as Supplementary Data. Also included with the Supplementary Data is a listing of a stand-alone FORTRAN subroutine for

Table 8. Values of Virial and Transport Property Coefficients for Ar_2 Calculated from the Empirical MLR$\{N_\beta = 4\}$ PEF.

Temp./K T [K]	Press.Vir B_2 [$cm^3\ mol^{-1}$]	Acou.Vir. β_{2a} [$cm^3\ mol^{-1}$]	Viscosity η [μPa·s]	Therm.Cond. λ [$mW\,m^{-1}\,K^{-1}$]	Self Diff. $D_{AA'}$ [$10^{-4} m^2\,s^{-1}$]	Therm.Diff. α_0
50.	−758.430	−1107.577	4.3415	3.3935	0.5776	0.1747
100.	−182.473	−180.458	8.1403	6.3578	2.2302	0.0370
150.	−86.132	−66.932	12.0751	9.4309	4.9578	0.0783
200.	−47.890	−23.949	15.8535	12.3840	8.6469	0.1513
250.	−27.621	−1.595	19.3835	15.1461	13.1869	0.2190
300.	−15.173	11.931	22.6668	17.7181	18.4930	0.2750
350.	−6.814	20.879	25.7322	20.1216	24.5020	0.3198
400.	−0.852	27.158	28.6121	22.3811	31.1660	0.3555
500.	7.002	35.218	33.9264	26.5525	46.3183	0.4066
750.	16.351	44.145	45.4624	35.6084	93.7742	0.4705
1000.	20.312	47.359	55.4817	43.4702	153.4896	0.4957
2000.	24.404	48.738	88.6133	69.4457	497.2741	0.5120
3000.	24.633	47.056	116.4097	91.2238	987.4387	0.5051
5000.	23.680	43.575	164.6509	129.0054	2348.9590	0.4882

generating our recommended MLR potential energy function and tabulations of the primary and secondary data that have been employed in the determination of the MLR PEF for the Ar_2 dimer.

Acknowledgements

This research has been supported by the Natural Sciences and Engineering Research Council of Canada by way of a 'Discovery' grant awarded to R.J.L.

I. APPENDIX: REVIEW OF AGREEMENT WITH EXPERIMENTAL DATA

Appendix A.1: Comparisons with spectroscopic data

Spectroscopic data are generally believed to provide the most precise information about the potential well and low-energy repulsive wall. However, previous work [57] tended to focus attention upon properties deduced from those data, such as the vibrational level spacings $\Delta G_{v+1/2}$ and rotational constants B_v, rather than directly upon the set of actual transition energies, as considered herein. We believe that this is likely the reason that the PEFs of Aziz [57] and Boyes [140] have DRMSD values that are significantly larger (by 4.6%, 7.0%, respectively) than those generated by our recommended MLR PEF (first row of Table 6), in spite of the fact that those derived properties were included in their fits. Similarly, the fact that the predictions generated from the PEF of Jäger *et al.* [15] yield a spectroscopic data $\overline{dd}$ value within 2% of that arising from our fitted MLR function provides strong confirmation of the accuracy of their ab initio PEF in the well region.

Appendix A.2: Comparison with virial data

Equation-of-state (pressure) and acoustic second virial coefficient measurements, especially if they are available over an extensive temperature range, also serve as important sources of data from which potential energy information may be extracted. However, as virial coefficients involve integrations over the atomic separation, r, they are typically sensitive to broader features of the interaction, such as the "volume" of the potential well.

A visual comparison between computed and experimental values of the pressure second virial coefficient, $B_2(T)$, is presented in Fig. 4. Computed curves were generated from the potential-fit PEF $\text{MLR}_{N_\beta=4}$ (whose repulsive wall was 'tuned' to improve agreement with transport property data), two previous empirical PEFs [57, 140] that were determined from fits to derived spectroscopic properties (such as $\Delta G_{v+\frac{1}{2}}$ and B_v values) plus virial and transport property data, and the two-parameter Tang-Toennies [141] model PEF.

On the scale of the main figure it is not possible to distinguish the levels of agreement between the computed and experimental values of $B_2(T)$. Moreover, as it is typically difficult to determine $B_2(T)$ with a precision better than $\pm 1\%$, it remains rather difficult to distinguish amongst most of the computed curves even on the expanded scale of the inset figure showing the 200-600 K temperature range data. It is clear, however, that the TT03 curve lies well outside the experimental uncertainties and that the Aziz HFD-ID curve (green dash-dot-dot curve) may be marginally distinguished from the Boyes HFD-ID curve and the two MLR curves. These visual distinctions are consistent with the $\overline{dd}$-values listed in the second row of Table 6.

The fact that the Boyes HFD-ID PEF, which *was not* fitted to pressure virial data, yields a $\overline{dd}$-value for those data that is actually smaller than the $\overline{dd}$-value for the Aziz HFD-ID PEF that *was* fitted to it, quantitatively supports the statement in subsection 3.2 that $B_2(T)$ and $\beta_{2a}(T)$ depend upon the PEF in much the same way. The $\overline{dd}$-values of 1.180 [15] and 1.689 [16] for the *ab initio* PEFs indicate that the computed curve obtained with the former ab initio PEF will give agreement with experimental $B_2(T)$ data that is similar to the level of agreement obtained for the

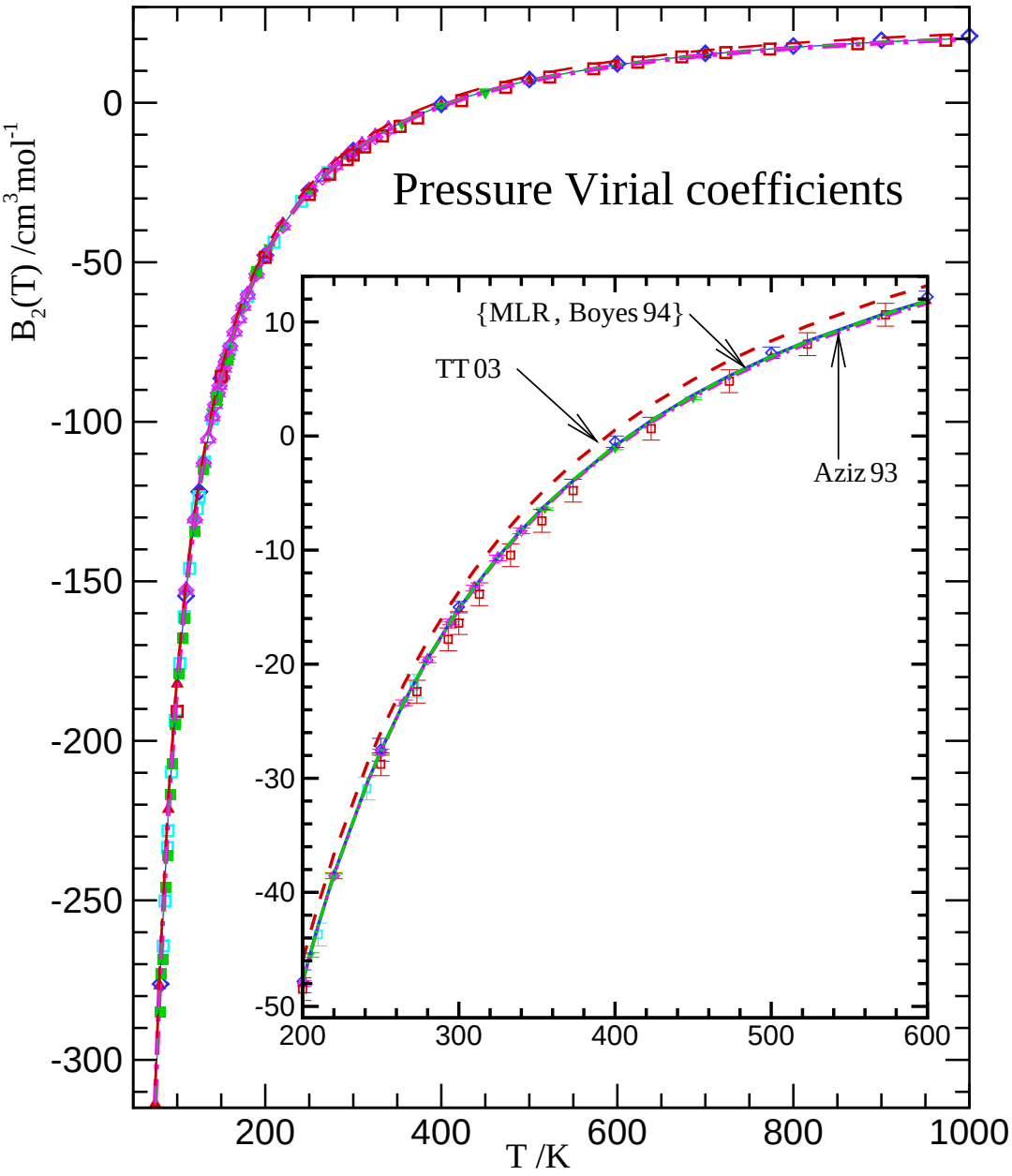

Figure 4. Temperature dependence of the equation-of-state (pressure) second virial coefficient. Computed curves: solid (blue), current MLR$_{N_\beta=4}$ PEF; dash-dot (magenta), Aziz93 [57] PEF; dash-dot-dot (green), Boyes94 [140] PEF; long-dash (red), TT03 [141] PEF. Experimental data: ▲ (red) [47]; ▼ (green) [85]; ◇ (blue) [83]; □ (cyan) [81]; △ (purple) [144]; ♢ (magenta) [84]; □ (red) [82]; ■ (green) [145].

present MLR empirical PEF, while the latter ab initio PEF will give agreement better than that obtained with the Aziz HFD-ID PEF but not as good as that obtained with the Boyes HFD-ID PEF.

Acoustic second virial coefficients, obtained from speed-of-sound measurements, can be determined with a precision that is at least ten times tighter than that associated with typical pressure virial coefficients. A visual comparison between the computed and experimental temperature dependence of the acoustic second virial coefficient, $\beta_{2a}(T)$, may be found in Fig. 5, while row 3 of

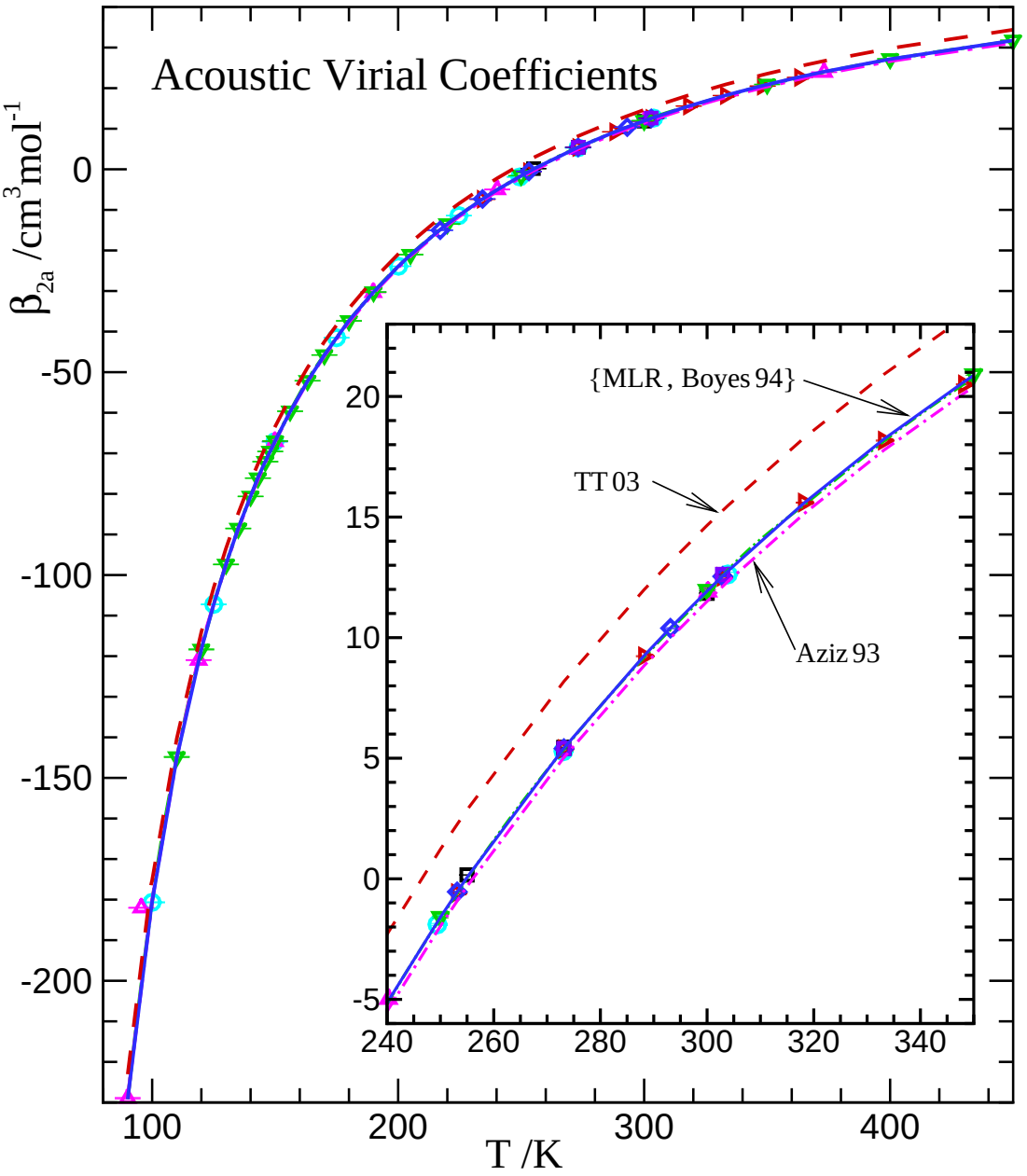

Figure 5. Temperature dependence of the acoustic second virial coefficient. Computed curves: solid (blue), current MLR$_{N_\beta=4}$ PEF; dash-dot (magenta), Aziz93 [57] PEF; dash-dot-dot (green), Boyes94 [140] PEF; long-dash (red), TT03 [141] PEF. Experimental data: ◯ (cyan) [46]; □ (black) [88]; △ (magenta) [47]; ▷ (red) [90]; ▽ (green) [89]; ◇ (blue) [54]; □ (purple) [45].

Table 6 shows the results of computations that were carried out for the same set of three empirical PEFs employed for the pressure virial comparisons in Fig. 4. It is already clear on the scale of the main panel of this figure that the $\beta_{2a}(T)$ curve computed from the two-parameter TT-model (with an acoustic virial $\overline{dd}$ value of 114.08) lies well outside the experimental uncertainties. Moreover, from the inset figure for the 240-350 K temperature range, it is also clear that the curve computed from the Aziz HFD-ID PEF (which did not include acoustic virial data in its determination) fails

to predict values of the acoustic second virial coefficient within the experimental uncertainties ($\overline{dd}$ value 15.290), while the curves computed from the Boyes HFD-ID PEF and the $\mathrm{MLR}_{N_\beta=4}$ PEF (both of which included the acoustic virial data in their determinations) remain visually indistinguishable on the expanded scale of the inset figure. The $\overline{dd}$ values for the entries 4 and 5 of row 3 of Table 6 then provide quantitative measures of the relative levels of agreement between the experimental data and the *ab initio* PEFs.

Appendix A.3: Comparison with transport data

Transport properties, whose calculation involves averages over the 'collision energy' (i.e., the centre-of-mass relative translational energy), are more strongly influenced by the nature of the repulsive wall of the PEF than are the spectroscopic or virial coefficient data. Indeed, a rough 'rule-of-thumb' estimate for the calculation of the appropriate thermally-averaged collision cross sections is that the thermal averaging over energy-dependent collision cross sections should be carried out for collision energies ranging from zero up to approximately ten times the thermal energy ($k_\mathrm{B}T$) associated with the highest temperature for which transport property measurements have been made. Thus, for example, for transport property measurements up to temperature $T = 1000$ K, appropriate collision cross section calculations in the range $0 \leq E_\mathrm{coll} \lesssim 7000\,\mathrm{cm}^{-1}$ will typically be required to determine the (converged) temperature dependence of transport coefficients.

The $\overline{dd}$-values listed in row 5 of Tables 4 and 6 have all been obtained from forward calculations of the transport coefficients using the various PEFs discussed above. As the overall transport data $\overline{dd}$-value of 1.061 obtained for the $\mathrm{MLR}_{N_\beta=4}$ PEF is close to unity (which means that the set of 609 computed values will, on average, lie just outside the corresponding assigned experimental uncertainties), there is thus little incentive for the incorporation of transport property data into the iterative nonlinear least-squares DPF package **dPotFit**, given that it would necessitate substantial revisions of the code package.

Expressions for the temperature dependence of the transport properties of a non-equilibrium monatomic gas may be found in a number of standard monographs (see, for example, [137, 146–148]): the simplest such expression may be referred to as the first Chapman-Cowling approximation. This first approximation is frequently a rather good one, especially for monatomic species, giving typically 98% or more of the converged value. Although second-approximation corrections generally suffice for typical experimental accuracies, so that higher-order calculations are seldom necessary, we have nonetheless carried out third-approximation computations of viscosity and thermal conductivity coefficients at all temperatures.

The first Chapman-Cowling approximation, $[\eta]_1$, for the viscosity of a monatomic gas is written simply as [147]

$$[\eta(T)]_1 \simeq \frac{k_\mathrm{B}T}{\overline{c}_\mathrm{r}\mathfrak{S}(20)} \tag{19}$$

in terms of an effective cross section $\mathfrak{S}(20)$, which depends upon the interaction PEF, and the average speed $\overline{c}_\mathrm{r} \equiv (8k_\mathrm{B}T/\pi m_\mathrm{r})^{\frac{1}{2}}$, with k_B the Boltzmann constant and m_r the reduced mass of the colliding pair of atoms. This first-order expression (19) may also be written in terms of the more

traditional omega integral $\Omega^{(2,2)}(T)$ using $\mathfrak{S}(20) = 8\Omega^{(2,2)}/(5\overline{c}_{\rm r})$ as [146]

$$[\eta(T)]_1 = \frac{5k_{\rm B}T}{8\Omega^{(2,2)}} \quad . \tag{20}$$

Higher-approximation expressions for the viscosity are then traditionally written as

$$[\eta(T)]_m = [\eta(T)]_1(1 + f_\eta^{[m]}) \,, \quad m \geq 2 \quad . \tag{21}$$

The most accurate experimental values for $\eta_{\rm Ar}$ have been obtained using dual-capillary instruments [101, 108–110] of the type developed by researchers at NIST [101]. Two of these measurements [108, 109], at temperature $T = 298.15\,{\rm K}$, have been assigned uncertainties of $\pm 0.0060\,\mu{\rm Pa\,s}$, corresponding to a precision of 0.022%. However, although both measurements, namely $22.5666 \pm 0.0060\,\mu{\rm Pa\,s}$ [108] and $22.5589 \pm 0.0060\,\mu{\rm Pa\,s}$ [109], fall within the uncertainty intervals assigned to the $T = 298.15\,{\rm K}$ values $22.570 \pm 0.019\,\mu{\rm Pa\,s}$ given in Ref. [101] and $22.562 \pm 0.014\,\mu{\rm Pa\,s}$ given in Ref. [110], their uncertainty intervals do not overlap. The current recommended empirical MLR PEF and the ab initio PEFs of Refs. [15, 16] all generate computed values of $\eta_{\rm Ar}$ that lie slightly below the confidence intervals of Refs. [101] and [108]. However, all three PEFs give $\eta_{\rm Ar}$ values that fall within the uncertainty interval of $\pm 0.014\,\mu{\rm Pa\,s}$ given in Ref. [110], while the $\eta_{\rm Ar}$ values generated by the MLR PEF and the ab initio PEF of Ref. [16] also lie within the tighter ($\pm 0.0060\,\mu{\rm Pa\,s}$) uncertainty interval of Ref. [109]. The measurements of May et al. [101] and Lin et al. [110] are for 18, respectively, 14 temperatures spanning temperature intervals $202\,{\rm K} < T < 395\,{\rm K}$, respectively, $298\,{\rm K} < T < 654\,{\rm K}$: the corresponding DRMSD ($\overline{dd}$) values for these two experimental data sets are ($\overline{dd}_{\rm May} = 0.950$, $\overline{dd}_{\rm Lin} = 0.840$), ($\overline{dd}_{\rm May} = 1.091$, $\overline{dd}_{\rm Lin} = 0.990$), and ($\overline{dd}_{\rm May} = 0.835$, $\overline{dd}_{\rm Lin} = 0.821$), respectively, for the MLR, ab initio [15], and ab initio [16] PEFs.

Figure 6 compares the temperature dependence of the viscosity coefficient of argon as computed (predicted) via its second Chapman-Cowling approximation using the four empirical PEFs of Table 6 with 226 experimental data spanning the temperature range $110\,{\rm K} \leq T \leq 1500\,{\rm K}$. The main panel shows the data from 110 K to 500 K while the two inset panels give comparisons for temperatures above 500 K. As was the case for the pressure and acoustic virial coefficients in Figs. 4 and 5, the only distinctly different curve on the scale of the main panel is that generated from the two-parameter TT03 model PEF [141].

It is clear from the inset panels that, particularly for higher temperatures, the two-parameter model of Ref. [141] does not successfully predict the viscosity of gaseous argon for temperatures much above 300 K, generating values of $\eta(T)$ that are significantly too small. The curve for the Aziz HFD-ID PEF can also be seen to separate from the curves generated from the Boyes HFD-ID and the present MLR$_{N_\beta=4}$ PEF, which remain indistinguishable even on the scale of the figure inserts. The Boyes HFD-ID and the present MLR$_{N_\beta=4}$ PEF may, however, be distinguished from one another by the $\overline{dd}$-values in the first row of Table 8. These $\overline{dd}$-values indicate that the MLR$_{N_\beta=5}$ PEF represents the viscosity data slightly better than does the Boyes HFD-ID PEF, while the next two entries show that the Jäger et al. *ab initio* PEF [15] represents the viscosity data about as well

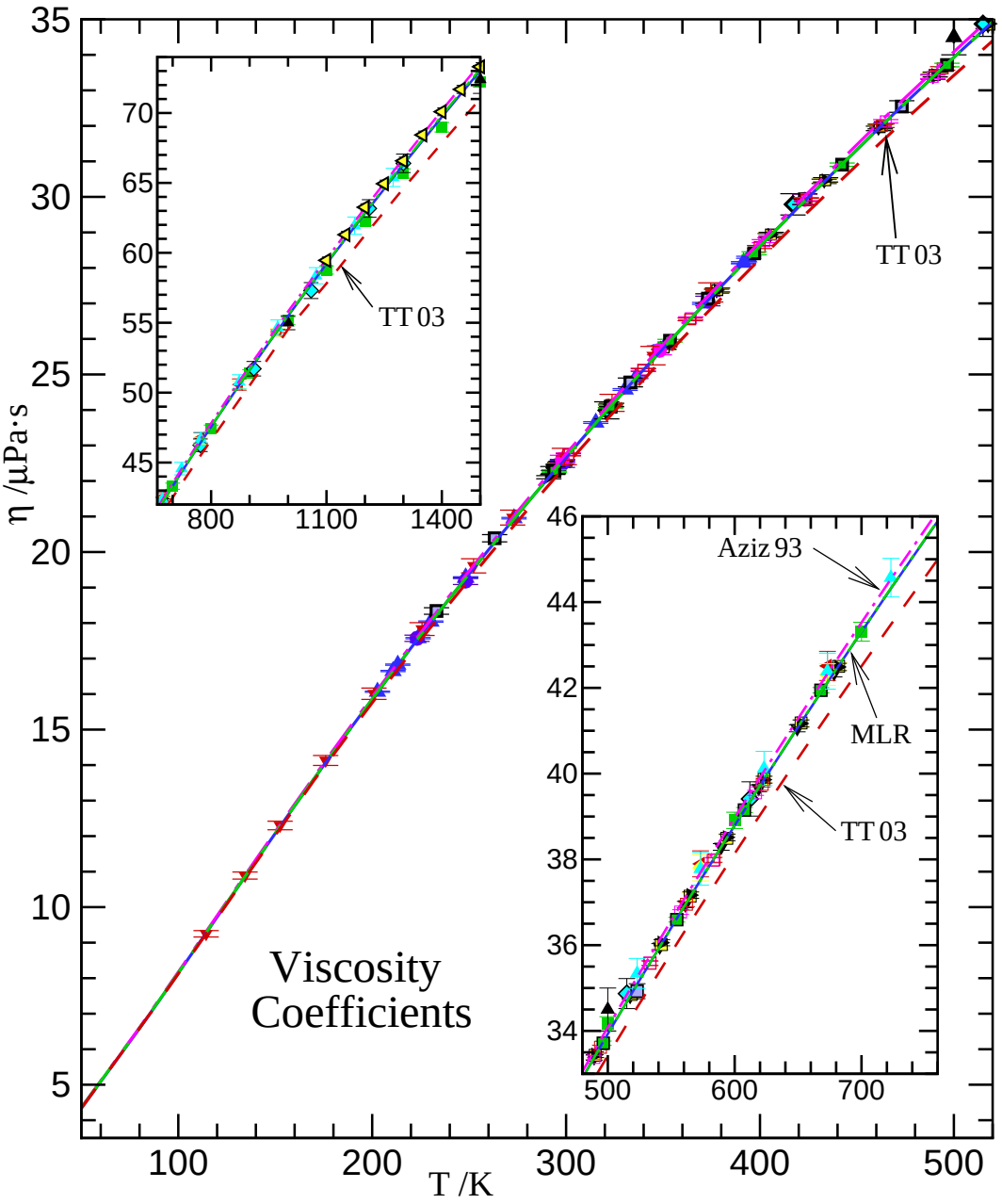

Figure 6. Temperature dependence of the shear viscosity coefficient. Computed curves: solid blue, current $\mathrm{MLR}_{N_\beta=4}$ PEF; dash-dot magenta, Aziz93 [57] PEF; dash-dot-dot green, Boyes94 [140] PEF; long-dash red, TT03 [141] model. Experimental data: ▲ (solid, blue) [101]; ▼ (solid, red) [97]; □ (hollow, mauve-filled) [107]; ▼ (solid, black), □ (hollow, yellow-filled), ► (solid, black), [105]; ◇ (hollow, cyan-filled) [103]; ● (solid, blue) [95]; ● (solid, magenta) [106]; ▲ (solid, black) [104]; □ (hollow, magenta), □ (hollow, red) [149]; □ (hollow, green-filled) [50]; ▲ (solid, cyan) [82].

as does the Boyes PEF, and that the viscosity values computed from the Patkowski-Szalewicz *ab initio* PEF [16] are comparable to those obtained using the $\mathrm{MLR}_{N_\beta=4}$ PEF. The final entry then shows that the two-parameter TT-model PEF represents these data quite poorly. Curves calculated from the two *ab initio* PEFs have not been included in any of Figs. $6-8$, as on the scales of those figures they are indistinguishable from the curves for the Boyes and $\mathrm{MLR}_{N_\beta=4}$ PEFs.

Table 9. $\overline{dd}$ Values for Individual Transport Properties.

		Potential Energy Function					
property	#data	$\mathrm{MLR}_{N_\beta=4}$	Aziz	Boyes	Jäger	Patk.	TT'03
Viscosity	236	0.817	2.066	0.853	0.856	0.822	5.832
Relative Viscosity	22	1.182	2.654	1.818	1.523	1.525	6.698
Thermal Conductivity	195	0.686	1.455	0.906	0.903	0.880	3.686
Isotopic Diffusion	55	0.750	1.090	0.935	0.823	0.831	1.270
Rel. Isotopic Diffusion	11	2.104	8.203	4.201	2.781	2.938	13.613
Thermal Diffusion	74	1.418	1.396	1.601	1.471	1.479	3.273
Overall Transport	593	0.926	2.063	1.188	1.059	1.052	4.959

An examination of the first Chapman-Cowling approximation for the shear viscosity of a monatomic gas, coupled with the natures of the set of Ar–Ar PEFs illustrated in Fig. 1, enables a correlation to be drawn between the temperature dependence of the viscosity coefficient calculated using these PEFs and the nature of the repulsive wall of the PEF. Such a comparison will suffice for this purpose, as higher approximations make only minor corrections to the values obtained using the first approximation expression: note that $f_\eta^{[3]}$ ranges from 0.0005 at 200 K to 0.0050 at 600 K to 0.0070 at 6000 K. It will thus be clear from Eq.(19) that for a given temperature T, a smaller value of η implies a larger value of $\mathfrak{S}(20)$: thus, for example, for $T = 700\,\mathrm{K}$ (in the lower inset panel of Fig. 6) the relative order of the calculated values of $\eta(700\mathrm{K})$ is $\mathrm{TT03} < \mathrm{MLR}_{N_\beta=4} \simeq \mathrm{Boyes} < \mathrm{Aziz}$. From the lower panel of Fig. 1, it is clear that all five PEFs and the TT03 model of Table 8 are roughly equivalent in the well region, while from the upper panel of Fig. 1 it is clear that the TT03 model is the most repulsive and the Aziz PEF is the least repulsive (although not by much more than the Boyes PEF), while the $\mathrm{MLR}_{N_\beta=4}$ PEF lies between the Boyes PEF and TT03 model.

Measurement of transport phenomena in a monatomic gas necessarily involves observation of different isotopes that are assumed to have identical pair potentials, but must formally be treated as different species. As is well known (see, e.g., Ref. [148] and references therein), transport phenomena are more complex for gas mixtures than for pure gases. In particular, for a binary mixture of gases A and B the energy and mass flux vectors $\mathbf{q}$ (heat flux) and $\mathbf{J}^{\mathrm{d}}$ (diffusive flux) may be written as [147, 148]

$$\mathbf{q} = -\lambda T \nabla \ln T - \frac{p}{x_{\mathrm{A}} x_{\mathrm{B}}} \widetilde{D}_{\mathrm{T}} \nabla x_{\mathrm{A}} \tag{22}$$

and

$$\mathbf{J}^{\mathrm{d}} \equiv \mathbf{v}_{\mathrm{A}} - \mathbf{v}_{\mathrm{B}} = -\frac{1}{x_{\mathrm{A}} x_{\mathrm{B}}} \left[D_{\mathrm{T}} \nabla \ln T + D_{\mathrm{BA}} \nabla x_{\mathrm{A}} \right] \tag{23}$$

in terms of the non-equilibrium thermodynamic driving forces $-\nabla \ln T$ and $-\nabla x_{\mathrm{A}}$ associated with temperature and mole-fraction (concentration) gradients maintained across the container. Four transport coefficients are required to describe these two fluxes: two diagonal linear response coefficients, specifically the thermal conductivity coefficient λ associated with the energy flux caused by the temperature gradient and the binary diffusion coefficient D_{BA} associated with the mass flux

associated with the mole-fraction (concentration) gradient, plus two off-diagonal linear response coefficients, specifically the better-known thermal diffusion coefficient $D_{\rm T}$ associated with a mass flux caused by the presence of the temperature gradient in the container and the lesser-known diffusion-thermal (or Soret) coefficient $\widetilde{D}_{\rm T}$ associated with the reciprocal effect, that is, an energy (heat) flux caused by the presence of a mole-fraction gradient in the container.

Figure 7 illustrates the level of agreement between the temperature dependence of the thermal conductivity coefficient as calculated from the second Chapman-Cowling approximation and its experimental temperature dependence. As for the viscosity coefficient, third Chapman-Cowling approximation corrections are relatively small, ranging from $f_\lambda^{[3]} \simeq 0.0008$ for $T \simeq 210\,{\rm K}$ to 0.0075 at 600 K to $\simeq 0.01$ at 2000 K. The main panel shows the comparison for the temperature range 250 K to 1250 K, while the two inset panels give comparisons for lower (100 K to 240 K) and higher (1000 K to 1950 K) temperatures. The $\lambda(T)$ curve computed using the two-parameter TT03 model falls significantly below the experimental values, especially for temperatures of 500 K or higher. Indeed, as can be seen from the third row of Table 8, the TT03 model has a DRMSD value of 3.686, while the three empirical PEFs and both *ab initio* PEFs generate DRMSD values near unity, ranging from 1.455 for the Aziz HFD-ID PEF to 0.686 for the $\text{MLR}_{N_\beta=4}$ PEF.

Note that the relative ordering of the computed values of $\lambda(T)$ is the same for a given temperature as that found for $\eta(T)$. That this should be so may also be seen from the first Chapman-Cowling approximation expression according to which $\lambda(T)$ may be written in terms of the effective cross sections $\mathfrak{S}(11)$ or $\mathfrak{S}(20)$, or in terms of the 'Omega integral' $\Omega^{(2,2)}$ [147]

$$[\lambda(T)]_1 \;=\; \frac{5k_{\rm B}^2T}{2m\,\overline{c}_{\rm r}\,\mathfrak{S}(11)} = \frac{15k_{\rm B}^2T}{4m\,\overline{c}_{\rm r}\,\mathfrak{S}(20)} \;=\; \frac{75k_{\rm B}^2T}{32m\,\Omega^{(2,2)}} \tag{24}$$

with m the mass of an (argon) atom, because of the exact relation $\mathfrak{S}(11) \;=\; \frac{2}{3}\,\mathfrak{S}(20)$ [147]. From Eq.(24) it will be clear that, apart from rather small differences associated with higher-approximation corrections, the relative abilities of the PEFs under consideration to represent the temperature dependence of the thermal conductivity coefficient of gaseous argon should be the same as that obtained for the viscosity coefficient. As may thus be anticipated, this conclusion is confirmed by an examination of the first and third rows of Table 8.

Figure 8 compares experimental values for the isotopic diffusion coefficient $D_{\rm A'A}(T)$ for ^{36}Ar (A′) diffusing through a dilute gas of ^{40}Ar (A) with values computed from the same set of three empirical PEFs and TT03 model that were shown in Figs. 6 and 7 for the temperature dependences of the viscosity and thermal conductivity coefficients. Values for $D_{\rm A'A}(T)$ have been computed using the second Kihara approximation for $f_D^{[2]}$ [137], as the Chapman-Cowling second approximation for this correction is considerably more complex and gives values that do not differ by much numerically from those obtained using the much simpler Kihara expression [137]. Values computed using the Kihara expression for $f_D^{[2]}$ range from 0.0001 at $T = 77\,{\rm K}$ to 0.0046 at 600 K to 0.0062 at 1600 K.

Note that because isotopic diffusion rates are rather difficult to measure accurately, and as naturally-occurring argon is almost isotopically pure ^{40}Ar (containing only 0.3365% ^{36}Ar and 0.0632% ^{38}Ar), isotopic diffusion in argon presents a particularly challenging case for the exper-

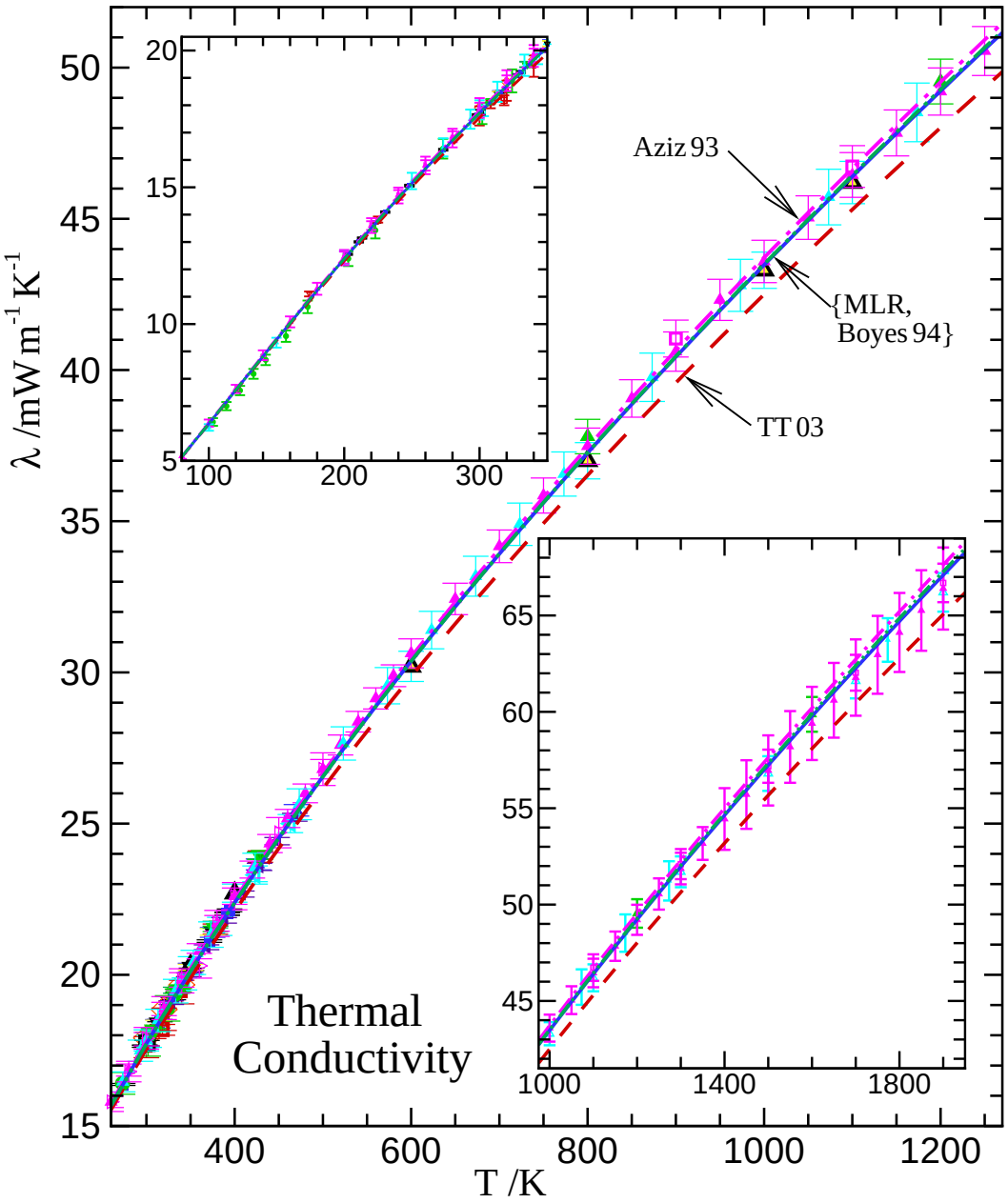

Figure 7. Temperature dependence of the thermal conductivity coefficient. Computed curves: solid blue, current MLR$_{N_\beta=4}$ PEF; dash-dot magenta, Aziz93 [57] PEF; dash-dot-dot green, Boyes94 [140] PEF; long-dash red, TT03 [141] model. Experimental data: ■ (solid, blue) [101]; ■ (solid, red) [123]; □ (hollow, magenta) [113]; □ (hollow, red) [117]; □ (hollow, black) [115]; ▼ (solid, green) [121]; ▼ (solid, red) [120]; ▲ (solid, magenta) [92]; ▲ (solid, cyan) [82]; ▲ (solid, green) [111]; ● (solid, green) [53]; ● (solid, blue) [119]; ● (solid, magenta) [118]; ◀ (solid, cyan) [122]; ◀ (solid, violet) [112]; ▽ (hollow, yellow-filled) [116]; ▷ (hollow, magenta) [93]; △ (hollow, green) [114]; ◇ (hollow, orange) [124].

imentalist. Only two direct experimental measurements have been carried out, one by Winn [132] in 1950 and one by De Paz et al. [133] in 1967. The experimental uncertainties are quite large, typically of the order of ±3%. Also shown in Fig. 8 are smoothed values of $D_{\mathrm{A'A}}(T)$ determined by Kestin et al. [82] from an experimental correlation. As may be seen from this figure, the temperature

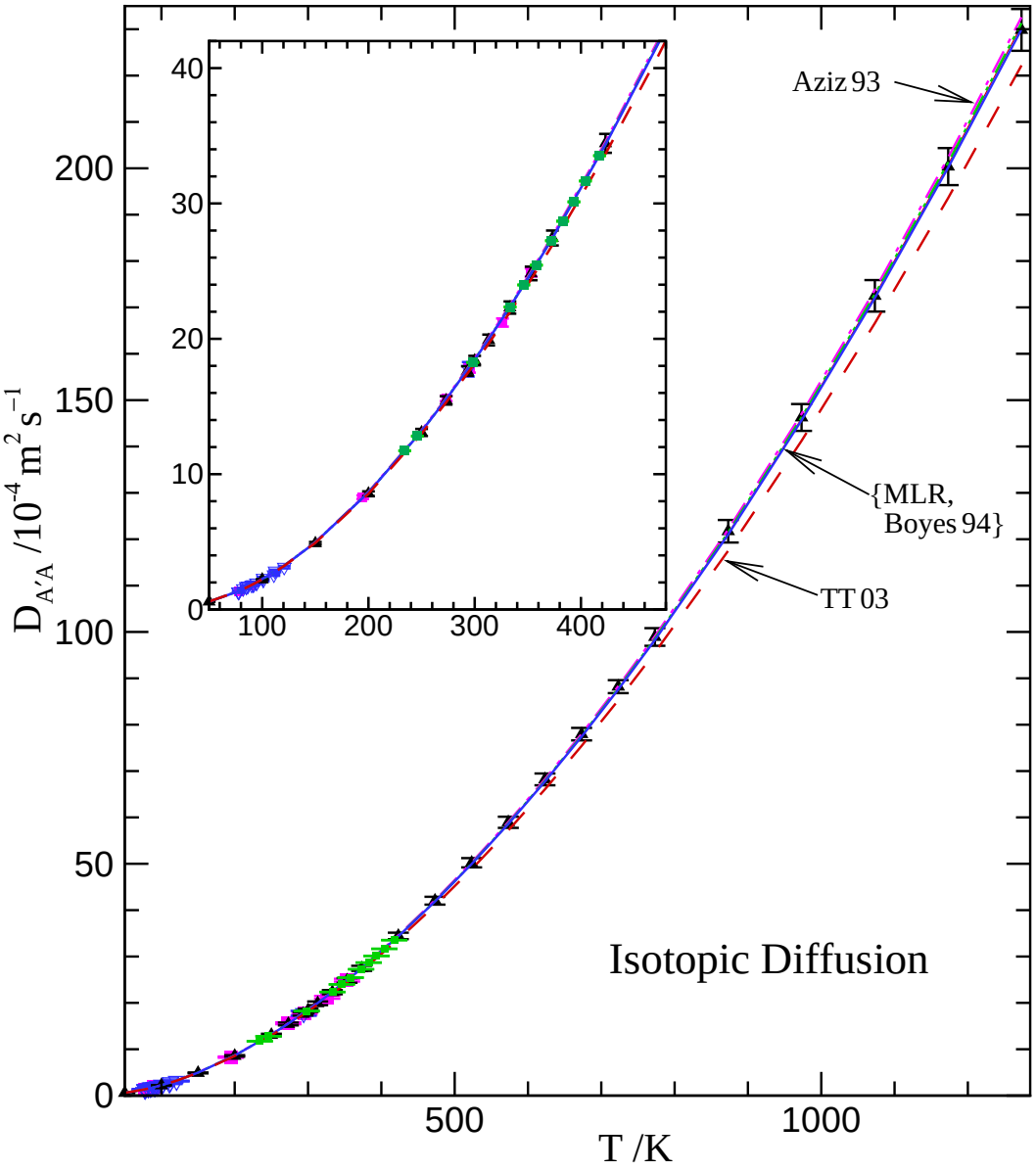

Figure 8. Temperature dependence of the isotopic-diffusion coefficient in Ar at pressure 1 bar. Computed curves: solid (blue), current $\mathrm{MLR}_{N_\beta=4}$ PEF; dash-dot (magenta), Aziz93 [57] PEF; dash-dot-dot (green), Boyes94 [140] PEF; long-dash (red), TT03 [141] model. Experimental data: ▼ (solid, blue) [133]; ■ (solid, magenta) [132]; ▲ (solid, cyan) [82]; ■ (solid, green) [134].

dependence predicted by the TT03 two-parameter model lies significantly below the experimental values, especially for temperatures above 500 K.

In 1969, Vugts, Boerboom, and Los [134] carried out relative measurements of the isotopic diffusion coefficient $D_{\mathrm{A'A}}(T)$ at ten temperatures in the range $234\,\mathrm{K} < T < 418\,\mathrm{K}$, with a reported uncertainty of ±0.1%. Their relative data have been converted into absolute data by employing their reference value $D_{\mathrm{A'A}} = 18.25 \pm 0.090\,\mathrm{cm^2\,s^{-1}}$ at $T = 298.15\,\mathrm{K}$, and are represented in Fig. 8 by solid green squares. Although it is difficult to discern on the scale of the figure, but it is clear

from Table 8, values of $D_{\mathrm{A'A}}(T)$ computed using the five PEFs and the TT03 model lie well outside the experimental uncertainties assigned to the measurements by Vugts et al. [134]: this suggests that the assignment of $\pm 0.1\%$ uncertainties to their data was likely overly optimistic.

As for the viscosity and thermal conductivity coefficients, the temperature dependence of $D_{\mathrm{A'A}}(T)$ predicted by computations based upon the Boyes HFD-ID and $\mathrm{MLR}_{N_\beta=4}$ PEFs are essentially indistinguishable on the scales of Fig. 8, while the $D_{\mathrm{A'A}}(T)$ curve computed using the HFD-ID PEF of Aziz [57] is marginally distinguishable from those computed using the other two empirical PEFs. Here, as has been seen for $\eta(T)$ and $\lambda(T)$ in Figs. 6 and 7, respectively, the results in row 4 of Table 8 show that the $\overline{dd}$ values for the isotopic diffusion experimental data set allow a ranking to be made of the predictions: in particular, the $\overline{dd}$ values for the two *ab initio* PEFs are only $8-10\%$ larger than that for the $\mathrm{MLR}_{N_\beta=4}$ PEF, and those for the Boyes and Aziz PEFs are 25 and 45% larger, respectively, and the TT03 model is 69% larger,

Because the binary diffusion coefficient D_{AB} depends only upon the unlike-atom interaction, no simplification of its expression in terms of effective cross sections (or equivalently, of omega integrals) is achieved for isotopic diffusion, for which the interaction energies between all atomic isotopes are identical within the Born-Oppenheimer approximation. The relative ordering of the curves representing the temperature dependence of the isotopic diffusion coefficient can thus be understood from the first Chapman-Cowling approximation for the binary diffusion coefficient which, for isotopic diffusion of A′ in A is given [147] by

$$D_{\mathrm{A'A}}(T) = \frac{k_{\mathrm{B}}T}{m_{\mathrm{A'}}} \, \frac{1}{n_{\mathrm{A}} \, \overline{c}_{\mathrm{A'A}} \, \mathfrak{S}(10|\mathrm{A'})_{\mathrm{A'A}}} \quad , \tag{25}$$

with $m_{A'}$ the mass of A', n_A the number density of A, $\overline{c}_{A'A}$ the average relative speed for $A'\,A$ collisions, and the effective cross section $\mathfrak{S}(10|\mathrm{A'})_{\mathrm{A'A}}$ for mass diffusion is related to the more traditional omega-integral $\Omega^{(1,1)}_{\mathrm{A'A}}$ by [147]

$$\mathfrak{S}(10|\mathrm{A'})_{\mathrm{A'A}} = \frac{16}{3\,\overline{c}_{\mathrm{A'A}}} \, y^2_{\mathrm{A}} \, \Omega^{(1,1)}_{\mathrm{A'A}} \quad , \tag{26}$$

with $y^2_{\mathrm{A}} \equiv m_{\mathrm{A}}/(m_{\mathrm{A}} + m_{\mathrm{A'}})$ a mass fraction. The relative ordering of the computed values of $D_{\mathrm{A'A}}(T)$ from smallest to largest at a given temperature T will be dictated by the values obtained for $\mathfrak{S}(10|\mathrm{A'})_{\mathrm{A'A}}$ or, equivalently, of $\Omega^{(1,1)}_{\mathrm{A'A}}$, from largest to smallest, precisely as for $\eta(T)$ and $\lambda(T)$.

The lowest non-zero approximation for the thermal diffusion coefficient, or equivalently, the thermal diffusion factor α_{T} related to D_{T} by $D_{\mathrm{T}} = x_{\mathrm{A}} x_{\mathrm{B}} \alpha_{\mathrm{T}}$, involves a rather complicated combination of effective cross sections or of omega integrals, mole fractions, and mass ratios (see, for example, Eq.(2.3-58) of Ref. [147] or Eq.(A5.2.36) of Ref. [137]). Some simplification does occur for isotopic atomic mixtures, as all interaction energies are the same (i.e., independent of the atomic masses), but the expression is still relatively complex. However, if the isotopes are sufficiently heavy that the mass ratio $R_M \equiv (m_{\mathrm{A}} - m_{\mathrm{A'}})/(m_{\mathrm{A}} + m_{\mathrm{A'}})$ is small, then to a good approximation (upon neglecting

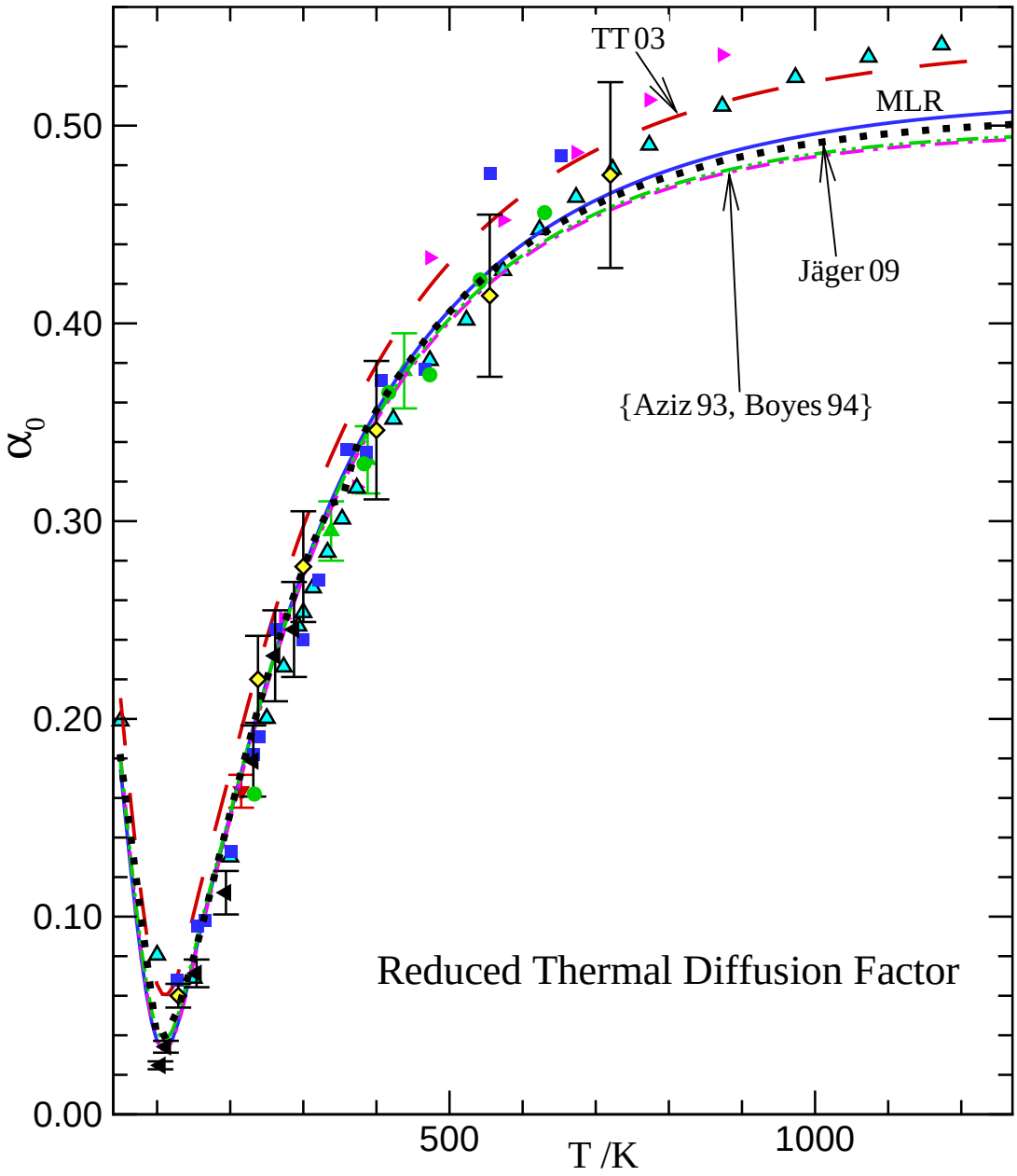

Figure 9. Temperature dependence of the reduced thermal diffusion coefficient α_0. Computed curves: solid (blue), $\text{MLR}_{N_\beta=4}$ PEF; dash-dot (magenta), Aziz [57] PEF; dash-dot-dot (green), Boyes [140] PEF; long-dash (red), TT'03 [141] model, dotted black, *ab initio* PEF of Jäger *et al.*. Experimental data: ▲ (solid, green) [130]; ▼ (solid, red) [131]; ▶ (solid, magenta) [129]; ▲ (solid, cyan) [82]; ■ (solid, blue) [127]; ◀ (solid, black) [128]; ● (solid, green) [126]; ♢ (black, yellow-filled) [125].

contributions of order R_M^2 or higher) the thermal diffusion factor can be written as [137, 146]

$$\alpha_{\mathrm{T}} \simeq \alpha_0 R_M \,, \tag{27}$$

in which α_0, which is independent of isotopic mixture composition, is referred to as the reduced thermal diffusion factor.

A comparison between 45 experimental values of the reduced thermal diffusion factor α_0 and the temperature dependences generated from the Chapman-Cowling first approximation expression for $[\alpha_0]_1$ and a second approximation correction using the Kihara expression for $f_\alpha^{[2]}$ for the empirical-fit PEFs is presented in Fig. 9. The second-approximation corrections are significantly larger for this cross-coefficient, ranging from 0.0034 for $T = 100\,\mathrm{K}$ to 0.0225 at 600 K to 0.035 at 1600 K. An additional 29 values of α_0 determined by Kestin et al. [82] based upon statistical least-squares-fits to experimental data have also been included in this figure, as have predictions of the temperature dependence of $[\alpha_0]_2$ based upon the TT03 two-parameter model PEF (dashed red curve) and the Jäger et al. [15] modified TT form PEF that was fitted to their *ab initio* pair-interaction energies (dotted black curve). As the isotopic thermal diffusion factor is extremely difficult to measure with high precision, the experimental uncertainties assigned to α_0 are typically between $\pm 5\%$ and $\pm 10\%$. However, in order not to clutter Fig. 9 unnecessarily, typical error bars have been shown only for the Stevens and De Vries [128], Rutherford [130] and Stier [125] data, and for the Taylor [131] datum at temperature 215 K. Note also that as the value reported by Stier for α_T at $T = 154\,\mathrm{K}$ appears to be erroneous, it has been omitted from Fig. 9.

[1] J .C. Maxwell, *Phil. Trans. Roy. Soc.* **157**, 49 (1867).
[2] J. E. (Lennard-)Jones, Proc. Roy. Soc. (London) A **206**, 441 (1924).
[3] J. E. (Lennard-)Jones, Proc. Roy. Soc. (London) A **206**, 463 (1924).
[4] R. A. Buckingham, Proc. Roy. Soc. (London) A **168**, 264 (1938).
[5] E. A. Mason, J. Chem. Phys. **22**, 169 (1954).
[6] P. M. Morse, Phys. Rev. **34**, 57 (1929).
[7] G. C. Maitland and E. B. Smith, Chem. Phys. Lett. **22**, 443 (1973).
[8] C. Douketis, G. Scoles, S. Marchetti, M. Zen, and A. J. Thakkar, J. Chem. Phys. **76**, 3057 (1982).
[9] K. T. Tang and J. P. Toennies, J. Chem. Phys. **80**, 3726 (1984).
[10] K.-C. Ng, W. J. Meath, and A. R. Allnatt, Chem. Phys. **32**, 175 (1978).
[11] K.-C. Ng, W. J. Meath, and A. R. Allnatt, Mol. Phys. **38**, 375 (1979).
[12] R. Hellmann, E. Bich, and E. Vogel, Mol. Phys. **105**, 3013 (2007).
[13] M. Jeziorska, W. Cencek, K. Patkowski, B. Jeziorski, and K. Szalewicz, J. Chem. Phys. **127**, 124303 (2007).
[14] R. Hellmann, E. Bich, and E. Vogel, Mol. Phys. **106**, 133 (2008).
[15] B. Jäger, R. Hellmann, E. Bich, and E. Vogel, Mol. Phys. **107**, 2181 (2009); erratum, *ibid*, **108**, 105 (2010).
[16] K. Patkowski and K. Szalewicz, J. Chem. Phys. **133**, 094304 (2010).
[17] J. L. Dunham, Phys. Rev. **41**, 713, 721 (1932).
[18] (a) R. Rydberg, Z. Physik **73**, 376 (1931); (b) O. Klein, Z. Physik **76**, 226 (1932); (c) R. Rydberg, Z. Physik **80**, 514 (1933); (d) A.L.G. Rees, Proc. Phys. Soc. **59**, 998 (1947).
[19] J. A. Coxon and P. G. Hajigeorgiou, J. Mol. Spectrosc. **150**, 1 (1991); Can. J. Phys. **70**, 40 (1992).
[20] J. F. Ogilvie, Proc. Roy. Soc. (London) A **378**, 287 (1981).
[21] A. A. Šurkus, R. J. Rakauskas, and A. B. Bolotin, Chem. Phys. Lett. **105**, 291 (1984).
[22] P. G. Hajigeorgiou and R. J. Le Roy, in *49th Ohio State University International Symposium on Molecular Spectroscopy* (Columbus, Ohio, 1994), paper WE04; J. Chem. Phys. **112**, 3949 (2000).
[23] R. J. Le Roy and R. D. E. Henderson, Mol. Phys. **105**, 663 (2007).
[24] R. J. Le Roy, N. Dattani, J. A. Coxon, A. J. Ross, P. Crozet, and C. Linton, J. Chem. Phys. **131**, 204309 (2009).
[25] R. J. Le Roy, C. C. Haugen, J. Tao, and H. Li, Mol. Phys. **109**, 435 (2011).
[26] R. J. Le Roy and A. Pashov, J. Quant. Spectrosc. Radiat. Transfer **186**, 210 (2016).
[27] R. J. Le Roy, Y. Huang, and C. Jary, J. Chem. Phys. **125**, 164310 (2006).
[28] R. D. E. Henderson, A. Shayesteh, J. Tao, C. C. Haugen, P. F. Bernath, and R. J. Le Roy, J. Phys. Chem. A **117**, 13373 (2013).
[29] J. A. Coxon and P. G. Hajigeorgiou, J. Quant. Spectrosc. Radiat. Transfer **151**, 133 (2015).
[30] Y.-S. Cho and R. J. Le Roy, J. Chem. Phys. **144**, 024311 (2016).
[31] N. Dattani and R. J. Le Roy, J. Mol. Spectrosc. **268**, 199 (2011).

[32] V. V. Meshkov, A. V. Stolyarov, M. C. Heaven, C. Haugen, and R. J. Le Roy, J. Chem. Phys. **140**, 064315 (2014).

[33] H. Knöckel, S. Rühmann, and E. Tiemann, J. Chem. Phys. **138**, 094303 (2013), erratum: *ibid* **138**, 189910 (2013).

[34] Y. Tanaka and K. Yoshino, J. Chem. Phys. **53**, 2012 (1970).

[35] R. J. Le Roy, J. Chem. Phys. **57**, 573 (1972).

[36] E. A. Colbourn and A. E. Douglas, J. Chem. Phys. **65**, 1741 (1976).

[37] P. R. Herman, P. E. LaRocque, and B. P. Stoicheff, J. Chem. Phys. **89**, 4535 (1988).

[38] M. V. Bobetic and J. A. Barker, Phys. Rev. B **2**, 4169 (1970).

[39] J. A. Barker, R. A. Fisher, and R. O. Watts, Mol. Phys. **21**, 657 (1971).

[40] G. C. Maitland and E. B. Smith, Mol. Phys. **22**, 861 (1971).

[41] J. A. Barker, W. Fock, and F. Smith, Phys. Fluids **7**, 897 (1964).

[42] J. A. Barker and M. L. Klein, Chem. Phys. Lett. **11**, 501 (1971).

[43] J. M. Parson, P. E. Siska, and Y. T. Lee, J. Chem. Phys. **56**, 1511 (1972).

[44] J. J. H. van den Biesen, R. M. Hermans, and C. J. N. van den Meijdenberg, Physica **115**, 396 (1982).

[45] M. R. Moldover and J. P. M. Trusler, Metrologia **25**, 165 (1988).

[46] M. B. Ewing, A. A. Owusu, and J. P. M. Trusler, Physica A **156**, 899 (1989).

[47] M. B. Ewing and J. P. M. Trusler, Physica A **184**, 415 (1992).

[48] J. Kestin, S. T. Ro, and W. A. Wakeham, J. Chem. Phys. **56**, 4119 (1972).

[49] D. W. Gough, G. P. Matthews, and E. B. Smith, J. Chem. Soc. Faraday Trans. 1 **72**, 645 (1976).

[50] E. Vogel, Ber. Bunsenges. Phys. Chem. **88**, 997 (1984).

[51] E. Bich and E. Vogel, Int. J. Thermophys. **12**, 27 (1991).

[52] H. M. Roder, R. A. Perkins, and C. A. Nieto de Castro, Int. J. Thermophys. **10**, 1411 (1989).

[53] R. A. Perkins, D. G. Friend, H. M. Roder, and C. A. Nieto de Castro, Int. J. Thermophys. **12**, 965 (1991).

[54] M. R. Moldover, S. J. Boyes, C. W. Meyer, and A. R. H. Goodwin, J. Res, Natl. Inst. Std. Tech. **104**, 11 (1999).

[55] R. A. Aziz and M. J. Slaman, Mol. Phys. **58**, 679 (1986).

[56] R. A. Aziz and M. J. Slaman, J. Chem. Phys. **92**, 1030 (1990).

[57] R. A. Aziz, J. Chem. Phys. **99**, 4518 (1993).

[58] G. Chałasiński, D. J. Funk, J. Simons, and W. H. Breckenridge, J. Chem. Phys. **87**, 3569 (1987).

[59] A. D. McLean, B. Liu, and J. A. Barker, J. Chem. Phys. **89**, 6339 (1988).

[60] D. E. Woon, J. Chem. Phys. **100**, 2838 (1994).

[61] T. Van Mourik, A. K. Wilson, and T. H. Dunning Jr., Mol. Phys. **96**, 529 (1999).

[62] B. Fernández and H. Koch, J. Chem. Phys. **109**, 10255 (1998).

[63] S. M. Cybulski and R. R. Toczylowski, J. Chem. Phys. **111**, 10520 (1999).

[64] P. Slavíček, R. Kalus, P. Paška, I. Odvásková, P. Hobza, and A. Malijevský, J. Chem. Phys. **119**, 2102 (2003).

[65] K. Patkowski, G. Murdachaew, C.-M. Fou, and K. Szalewicz, Mol. Phys. **103**, 2031 (2005).

[66] E. Mason and T. Spurling, in *International Encyclopedia of Physical Chemistry and Chemical Physics, Topic 10, "The Fluid State"*, edited by J. Rowlinson (Pergamon Press, Oxford, 1969), Vol. 2, Chap. 2, pp. 17–66.

[67] J. P. M. Trusler, *Physical Acoustics and Metrology of Fluids* (Hilger, Bristol, 1991).

[68] M. R. Moldover, K. A. Gills, J. J. Hurly, J. B. Hehl, and J. Wilhelm, *Acoustic Measurements in Gases.* Chapter 10 of "Modern Acoustical Techniques for the Measurement of Mechanical Properties", Eds. M. Levy, H. E. Bass, R. Stern, **Vol. 39** "Experimental Methods in the Physical Sciences" (Academic Press, New York, 2001).

[69] F. R. W. McCourt, *Virial Coefficients*, Chapter 27, pp. 673-711 of "Handbook of Molecular Physics and Quantum Chemistry", S. Wilson Editor, Volume 3: *Molecular Physics in the Physicochemical Environment: Spectroscopy, Dynamics and Bulk Properties*, P. F. Bernath, Volume Editor, Wiley (2003).

[70] B. Foreman, P. K. Rol, and K. P. Coffin, J. Chem. Phys. **61**, 1658 (1974).

[71] R. A. Aziz. *Interatomic Potentials for Rare-Gases: Pure and Mixed Interactions*, Chapter 2 (pp. 5-86) in 'Inert Gases: Potentials, Dynamics, and Energy Transfer in Doped Crystals', Springer Series in Chemical Physics, Vol. 34, Ed. M. L. Klein, Spinger-Verlag, Berlin (1984).

[72] R. J. Le Roy, J. Quant. Spectrosc. Radiat. Transfer **186**, 179 (2016).

[73] J. A. Coxon and P. G. Hajigeorgiou, J. Mol. Spectrosc. **150**, 1 (1991).

[74] H. Richter, H. Knöckel, and E. Tiemann, Chem. Phys. **157**, 217 (1991).

[75] R. Brühl, J. Kapetanakis, and D. Zimmermann, J. Chem. Phys. **94**, 5865 (1991).

[76] J. A. Coxon and P. G. Hajigeorgiou, J. Mol. Spectrosc. **139**, 84 (1990).

[77] P. G. Hajigeorgiou and R. J. Le Roy, J. Chem. Phys. **112**, 3949 (2000).

[78] E. G. Lee, J. Y. Seto, T. Hirao, P. F. Bernath, and R. J. Le Roy, J. Mol. Spectrosc. **194**, 197 (1999).

[79] A. Michels, H. U. B. Wijker, and H. K. Wijker, Physica **15**, 627 (1949).

[80] A. Michels, J. M. Levelt, and W. De Graaff, Physica **24**, 659 (1958).

[81] M. A. Byrne, M. R. Jones, and L. A. K. Staveley, Trans. Faraday Soc. **64**, 1747 (1968).

[82] J. Kestin, K. Knierim, E. A. Mason, B. Najafi, S. T. Ro, and M. Waldman, J. Phys. Chem. Ref. Data **13**, 229 (1984).

[83] R. M. Sevast'yanov and R. A. Chernyavskaya, Inzh.-Fiz. Zh. **52**, 974 (1987).

[84] R. Gilgen, R. Kleinrahm, and W. Wagner, J. Chem. Thermo. **26**, 383 (1994).

[85] A. F. Estrada-Alexanders and J. P. M. Trusler, Int. J. Thermophys. **17**, 1325 (1996).

[86] J. Klimeck, R. Kleinrahm, and W. Wagner, J. Chem. Thermo. **30**, 2571 (1998).

[87] W. Cencek, G. G. A. H. Harvey, M. O. McLinden, and K. Szalewicz, J. Phys. Chem. A **117**, 7542 (2013).

[88] M. B. Ewing and A. R. H. Goodwin, J. Chem. Thermo. **24**, 531 (1992).

[89] A. F. Estrada-Alexanders and J. P. M. Trusler, J. Chem. Thermo. **27**, 1075 (1995).

[90] G. Benedetto, R. M. Gavioso, R. Spagnolo, P. Marcarino, and A. Merlone, Metrologia **41**, 74 (2004).

[91] J. H. Dymond, K. N. Marsh, R. C. Wilhoit, and K. C. Wong, Landolt-Börnstein, New Series, Group IV: Physical Chemistry, **21A**, *Virial Coefficients of Pure Gases.* (Springer, Berlin, 2002).

[92] H. Ziebland, Pure and Applied Chemistry **53**, 1863 (1981).
[93] B. A. Younglove and H. J. M. Hanley, J. Phys. Chem. Ref. Data **15**, 1323 (1986).
[94] H. L. Johnston and E. R. Grilly, J. Phys. Chem. **46**, 948 (1942).
[95] G. P. Flynn, R. V. Hanks, N. A. Lemaire, and J. Ross, J. Chem. Phys. **38**, 154 (1963).
[96] J. Kestin and A. Nagashima, J. Chem. Phys. **40**, 3648 (1964).
[97] A. G. Clarke and E. B. Smith, J. Chem. Phys. **48**, 3988 (1968).
[98] J. A. Gracki, G. P. Flynn, and J. Ross, J. Chem. Phys. **51**, 3856 (1969).
[99] F. A. Guevara, B. B. McInteer, and W. E. Wageman, Phys. Fluids **12**, 2493 (1969).
[100] R. A. Dawe and E. B. Smith, J. Chem. Phys. **52**, 693 (1970).
[101] E. F. May, R. F. Berg, and M. R. Moldover, Int. J. Thermophys. **28**, 1085 (2007).
[102] J. Hellmans, J. Kestin, and S. Ro, Physica **71**, 1 (1974).
[103] A. A. Clifford, P. Gray, and A. C. Scott, J. Chem. Soc. Faraday Trans. 1 **71**, 875 (1975).
[104] N. B. Vargaftik and Y. D. Vasilevskaya, J. Eng. Phys. **46**, 30 (1984).
[105] E. Vogel, Int. J. Thermophys. **31**, 447 (2010).
[106] J. Wilhelm and E. Vogel, Int. J. Thermophys. **21**, 301 (2000).
[107] C. Evers, H. W. Lösch, and W. Wagner, Int. J. Thermophys. **23**, 1411 (2002).
[108] R. F. Berg and M. R. Moldover, J. Phys. Chem. Ref. Data **41**, 043104 (2012).
[109] R. F. Berg and W. C. Burton, Mol. Phys. **111**, 195 (2013).
[110] H. Lin, X. J. Feng, J. T. Zhang, and C. Liu, J. Chem. Phys. **141**, 234311 (2014).
[111] F. M. Faubert and G. S. Springer, J. Chem. Phys. **57**, 2333 (1972).
[112] J. W. Haarman, AIP Conf. Proc. **11**, 193 (1973).
[113] G. Ś. Springer and E. W. Wingeier, J. Chem. Phys. **59**, 2747 (1973).
[114] S. H. P. Chen and S. C. Saxena, Mol. Phys. **29**, 455 (1975).
[115] R. Fleeter, J. Kestin, R. Paul, and W. A. Wakeham, Physica A **108**, 371 (1981).
[116] A. A. Clifford, P. Gray, A. I. Johns, A. C. Scott, and J. T. R. Watson, J. Chem. Soc. Faraday Trans. 1 **77**, 2679 (1981).
[117] J. Kestin, S. T. Ro, and W. A. Wakeham, Ber. Bunsenges. Phys. Chem. **86**, 753 (1982).
[118] K. N. Haran, G. C. Maitland, M. Mustafa, and W. A. Wakeham, Ber. Bunsenges. Phys. Chem. **87**, 657 (1983).
[119] A. I. Johns, S. Rashid, and J. T. R. Watson, J. Chem. Soc. Faraday Trans. 1 **82**, 2235 (1986).
[120] U. V. Mardolcar, C. A. Nieto de Castro, and W. A. Wakeham, Int. J. Thermophys. **7**, 259 (1986).
[121] J. Millat, M. Mustafa, M. Ross, W. A. Wakeham, and M. Zalaf, Physica A **145**, 461 (1987).
[122] W. Hemminger, Int. J. Thermophys. **8**, 317 (1987).
[123] H. M. Roder, R. A. Perkins, and A. Laesecke, J. Res, Natl. Inst. Std. Tech. **105**, 221 (2000).
[124] L. Sun and J. E. S. Venart, Int. J. Thermophys. **26**, 325 (2005).
[125] L. G. Stier, Phys. Rev. **62**, 548 (1942).
[126] T. I. Moran and W. W. Watson, Phys. Rev. **109**, 1184 (1958).
[127] R. Paul, A. J. Howard, and W. W. Watson, J. Chem. Phys. **39**, 3053 (1963).
[128] G. A. Stevens and A. E. De Vries, Physica **39**, 346 (1968).

[129] W. L. Taylor and S. Weissman, J. Chem. Phys. **59**, 1190 ((1973); *erratum*, **62**, 3837 (1975)).

[130] W. M. Rutherford, J. Chem. Phys. **58**, 1613 (1973).

[131] W. L. Taylor, J. Chem. Phys. **62**, 3837 (1975).

[132] E. B. Winn, Phys. Rev. **80**, 1024 (1950).

[133] M. De Paz, B. Turi, and M. L. Klein, Physica **36**, 127 (1967).

[134] H. F. Vugts, A. J. H. Boerboom, and J. Los, Physica **44**, 219 (1969).

[135] A. Kumar and A. J. Thakkar, J. Chem. Phys. **132**, 074301 (2010).

[136] C. Hättig and B. A. Hess, J. Phys. Chem. **100**, 6243 (1996).

[137] G. C. Maitland, M. Rigby, E. B. Smith, and W. A. Wakeham, *Intermolecular Forces - Their Origin and Determination* (Oxford University Press, Oxford, UK, 1981).

[138] A. Kramida, Yu. Ralchenko, J. Reader, and NIST ASD Team (2015). NIST Atomic Spectra Database (ver. 5.3), [Online]. Available: http://physics.nist.gov/asd [2016, September 13]. National Institute of Standards and Technology, Gaithersburg, MD.

[139] R. J. Le Roy, J. Mol. Spectrosc. **191**, 223 (1998).

[140] S. J. Boyes, Chem. Phys. Lett. **221**, 467 (1994).

[141] K. T. Tang and J. P. Toennies, J. Chem. Phys. **118**, 4976 (2003).

[142] Although it is clear from the discussion presented in Ref. [16] that uncertainties for the results in Ref. [15] should, in principle, be larger than those determined in Ref. [16], the assignment of larger uncertainties here would only serve to introduce an unwarranted bias in favour of the results reported in Ref. [15].

[143] V. V. Meshkov, A. V. Stolyarov, and R. J. Le Roy, J. Chem. Phys. **135**, 154108 (2011).

[144] C. Tegeler, R. Span, and W. Wagner, J. Phys. Chem. Ref. Data **28**, 779 (1999).

[145] R. D. Weir, I. Jones, J. S. Rowlinson, and G. Saville, Trans. Faraday Soc. **63**, 1320 (1967).

[146] S. Chapman and T. G. Cowling, *Mathematical Theory of Nonuniform Gases, 3rd Ed.* (Cambridge University Press, London, UK, 1970).

[147] F. R. W. McCourt, J. J. M. Beenakker, W. E. Köhler, and I. Kuščer, *Nonequilibrium Phenonema in Polyatomic Gases* (Oxford University Press, Oxford, U,K., 1990), Vol. 1.

[148] F. R. W. McCourt, *Gas Transport Properties*, Chapter 28, pp. 712–752 of "Handbook of Molecular Physics and Quantum Chemistry", S. Wilson Editor, Volume 3: *Molecular Physics in the Physico-chemical Environment: Spectroscopy, Dynamics and Bulk Properties*, P. F. Bernath, Volume Editor, Wiley (2003).

[149] E. Vogel, Ber. Bunsenges. Phys. Chem. **21(M2)**, 169 (1972).